230 (2023) 212183

Contents lists available at ScienceDirect

Geoenergy Science and Engineering

journal homepage: www.sciencedirect.com/journal/geoenergy-science-and-engineering

Advanced modeling of diffusion and convection in multiphase compositional simulation for tight porous media

Sofiane H. Achour, Ryosuke Okuno *

The University of Texas at Austin, USA

ARTICLE INFO

Keywords:
Tight porous media
Diffusion
Sorption
Dusty gas model
Potential theory
Enhanced oil recovery

ABSTRACT

Small pore sizes influence the mass transport in gas enhanced oil recovery (EOR) in tight formations through complex phenomena such as diffusion and sorption. However, conventional simulators use relatively simple models for diffusion and sorption that do not properly represent non-ideal fluid interactions at high pressures. This paper presents a novel implementation of coupled diffusion and convection for multicomponent transport via the sorbed and bulk regions in tight porous media. Case studies highlight the important implication of convection in diffusion-dominant compositional transport in tight porous media.

The simulator uses multicomponent diffusion based on the dusty-gas model (DGM), which uses the fugacity gradient as the driving force. The adsorption model used is an approximate solution based on the Multicomponent Potential Theory of Adsorption (MPTA) using the sorbed and central regions. The capillary pressure is included both in the flow equations and the flash calculations by minimizing the Helmholtz free energy using the Peng-Robinson equation of state at a fixed temperature, pore volume, and overall composition.

A case study presents CO_2 injection into a 1-D tight porous medium with a ternary mixture of methane, n-butane, and n-decane as the initial oil. Before CO_2 injection, n-decane is most attracted to the pore wall and contained at a high concentration in the sorbed region. During CO_2 injection, CO_2 displaces n-decane from the pore wall, causing the counter-current transport of CO_2 and n-decane.

Simulation results show that the mixing of reservoir oil with CO_2 in small pores results in local pressure changes, which tend to drive both diffusion and convection. In all cases, convection enhances multicomponent transport by dissipating these pressure changes. When CO_2 is strongly attracted to the pore walls, a large pressure change on mixing accelerates the CO_2 diffusion into the reservoir through the sorbed region and also the counter-current transport of oil components through the central region.

1. Introduction

Although tight formations tend to result in inefficient oil recovery, they contributed more than 50% of domestic oil production in 2021 (Energy Information Administration, 2022; Clark, 2009; Lund, 2014). Efforts in CO_2 emission reduction in the energy industry caused renewed global interest in technologies to improve tight oil recovery without having to drill new wells; in particular, CO_2 injection can be a measure of carbon utilization and sequestration.

However, interactions between the reservoir fluids and walls of small pores in tight reservoirs cause various deviations from the theory of gas injection established for conventional reservoirs. In particular, these interactions affect phase behavior through capillary pressure, the relative importance of diffusion to convection, and sorption. This paper is part of an ongoing project of developing the Tight Reservoir Simulator "TigReS" that can properly account for all these phenomena (Achour and Okuno, 2020, 2021, 2022, 2023).

The most commonly used models for diffusion in tight reservoirs are Fick's law (Akkutlu and Fathi, 2012; Cronin et al., 2019, 2021; Yanze and Clemens, 2012) and Maxwell Stefan (Hoteit, 2013; Shojaei and Jessen, 2014; Mohebbinia and Wong, 2017). Achour and Okuno (2022) showed that Fick's law neglects the impact of non-ideal mixing as its fundamental assumption, and Maxwell-Stefan models can result in inconsistent pressure change owing to non-ideal mixing of injected solvents with reservoir fluid. Then, they used the dusty-gas model (DGM), a modified version of the Maxwell-Stefan model that includes Knudsen diffusion. Achour and Okuno (2022) presented a detailed analysis of multicomponent diffusion predicted by their model in a 1-D

* Corresponding author.Department of Petroleum and Geosystems Engineering, 200 E. Dean Keeton Street, Stop C0300, Austin, TX, 78712, USA.
E-mail addresses: sachour@utexas.edu (S.H. Achour), okuno@austin.utexas.edu (R. Okuno).

https://doi.org/10.1016/j.geoen.2023.212183
Received 13 April 2023; Received in revised form 1 July 2023; Accepted 23 July 2023
Available online 25 July 2023

reservoir model. Also, the DGM has been used to study solvent injection theory (Ma and Emami-Meybodi, 2022) and simulate enhanced oil recovery in a reservoir simulator (Olorode et al., 2021).

Sorption is the interaction between fluid molecules and the pore walls that causes a composition and density distribution across the pore. The excess sorbed amount is the additional number of moles near the pore wall due to sorption. Sorption has been studied for shale gas or coalbed methane reservoirs. For tight/shale oil reservoirs, it has been shown to cause light and heavy components to segregate between the central and near-wall regions of a pore (Baek and Akkutlu, 2019; Achour and Okuno, 2023). However, the impact of such compositional segregation on the transport mechanisms is not entirely clear yet; Baek and Akkutlu (2019) conducted equilibrium molecular dynamics simulations without transport, whereas Achour and Okuno (2023) neglected any impact of convection.

The Multicomponent Langmuir model is the most commonly used model for sorption; however, it predicts the excess amount with a monotonically increasing function of pressure (Butt et al., 2003), which Achour and Okuno (2023) described as a fundamental failure of the Multicomponent Langmuir. They then used an approximation of the Multicomponent Potential Theory of Adsorption (MPTA) originally developed by Shapiro and Stenby (1998). The traditional MPTA method solves for the composition and density distributions that yield a gradient in chemical potential for each component across a pore discretized into many regions from the pore wall to the pore center. The approximation of Achour and Okuno (2023) discretized the pore volume into two concentric regions labeled as the central and sorbed regions, for their flow simulator to efficiently compute the diffusive flux in both regions using the DGM. Results showed that sorption plays an important role in multicomponent diffusion because it enhanced countercurrent transport of species by allowing for compositional segregation in the two regions depending on the affinities of species for the pore wall.

Two main questions remain unanswered. Firstly, methane and CO_2 have different phase behavior and interactions with pore walls. Therefore, it is not clear whether the previous analysis on methane injection applies when CO_2 is used as a solvent. Secondly, convection was neglected in Achour and Okuno (2023) even though their results showed that the mixing of the reservoir oil with the injected solvent altered local pressures in the reservoir model. This paper aims to address these questions as part of the investigation.

The overall objective of this paper is to analyze the effect of sorption on compositional transport during CO_2 injection into tight porous media. The in-house simulator used in this paper accounts for sorption using the approximated MPTA method (Achour and Okuno, 2023) in each discretized pore consisting of two regions with their fixed volumes. It computes the equilibrium across the pore by iteratively changing the number of moles in each region to minimize the Helmholtz free energy. The flash calculations assume a fixed volume, temperature, and number of moles, and include the effect of capillary pressure (Achour and Okuno, 2021). The simulator computes thermodynamic fluid properties and diffusion coefficients using the Peng-Robinson equation of state (PREOS) (Robinson and Peng, 1978) in both regions and the DGM (Achour and Okuno, 2022). The simulator computes the multiphase Darcy convective flow using the LBC model (Lohrenz et al., 1964) for viscosity and STONE2 (Ertekin et al., 2001) for relative permeability. The main novelty of this paper lies in the implementation of coupled diffusion and convection for multicomponent transport via the sorbed and central regions in tight porous media. Achour and Okuno (2023) presented the application of the dusty gas model for diffusion with no convection; however, this paper shows the impact of convection on compositional transport in tight porous media, which is particularly important for CO_2 injection as will be shown in the case studies.

The simulation cases in this paper focus on shales because of the availability of relevant experimental data. However, tight sandstone and carbonate reservoirs are not excluded from the discussion presented in this paper because their small pores have a greater surface-area-to-volume ratio, which determines the impact of sorption on phase behavior and transport.

2. Methods

This section presents the formulation for solving the flow and mass transfer equations across a 1-D tight porous medium in our in-house Tight Reservoir Simulator or TigReS. This simulator accounts for the interactions between the fluid molecules and the pore walls by splitting pores into concentric regions of different compositions and densities. The equilibrium properties of each region are calculated using the MPTA approximation (Achour and Okuno, 2023), which is briefly described in the first part. The second part of this section presents specific details of how TigReS computes the compositional transport.

2.1. Equilibrium calculation

The traditional MPTA method was originally formulated by Shapiro and Stenby (1998) for calculating the composition and density profiles across a pore discretized with many discrete regions between the pore wall and the pore center. The approximation used in TigReS (Achour and Okuno, 2023) consists of only 2 discrete regions that model the pore, namely, the central (C) and sorbed regions (S). The calculation solves the N_c equations

$$\ln f_{i,S} - \frac{\varepsilon_{i,S}}{RT} = \ln f_{i,C}, \tag{1}$$

where i = 1,…,Nc for N_c components subject to four constraints as described below. R, T, $f_{i,C}$,$f_{i,S}$, and $\varepsilon_{i,S}$ are the universal gas constant, the temperature, the fugacities for component i in the central and sorbed regions, and the wall potential for component i.

The first two constraints are the mole balance

$$n_i = n_{i,C} + n_{i,S}, \tag{2}$$

where i = 1,…,Nc and volume balance

$$V = V_C + V_S \tag{3}$$

where n_i, V, $n_{i,r}$ and V_r are the total number of moles of component i, the total pore volume, the number of moles of component i in region r, and the volume of region r. The remaining constraints enforce a minimum number of moles,

$$n_{i,r} > 0, \tag{4}$$

where i = 1,..., N_C and r = 1,..., N_r, and a minimum molar volume,

$$\sum_{i=1}^{N_c} n_{i,r} b_i < V_r, \text{ where } r = 1, \ldots, N_r. \tag{5}$$

In the above, b_i is the co-volume parameter for the cubic equation of state assuming van der Waals' mixing rules.

The case studies presented in this paper use the Dubinin-Radushkevich-Astakhov (DRA) (Dubinin, 1985) wall potential model

$$\varepsilon_i(z) = \varepsilon_{i,0}\left(\ln\left(\frac{z_0}{z}\right)\right)^{1/\beta},$$

where i = 1,…,Nc, $\varepsilon_{i,0}$ and β are component specific and general calibration parameters, respectively, and z_0 and z are the total measured pore volume per unit mass of rock and the total volume per unit mass of rock between a point in the pore and the pore wall such that $z \in [0, z_0]$. The wall potential for component i of the sorbed region occupying a pore volume fraction of $S_S = V_S/V$ is calculated using the integral average

$$\varepsilon_{iS} = \frac{1}{S_S z_0} \int_0^{S_S z_0} \varepsilon_i(z) dz,$$

where i = 1,…,Nc. More detailed explanations of the algorithm and formulation are given by Achour and Okuno (2022).

The volume fractions of both regions in this 2-region approximated MPTA method are adjusted to best approximate the 100-region version. First, the 100 region MPTA method is computed at the reservoir pressure and temperature at a set of uniformly distributed points in composition space. At each composition, the pore is split into two pseudo-regions such that the one adjacent to the pore wall contains 80% of the excess moles per mass of solid rock defined as

$$\frac{n^{ex}}{m_s} = \int_{z_1}^{z_2} \rho - \rho_0 dz \tag{6}$$

for a pseudo-region extending from z_1 to z_2.

2.2. Flow simulation

This section describes the models used to compute the viscous part of compositional flow for the central region. The specific methods to compute the diffusive part based on the DGM (Achour and Okuno, 2022) in the central and sorbed regions are explained in detail in Achour and Okuno (2023).

TigReS computes the flow at each time step by solving the mole balance equations below using a partially implicit method, where the fugacities and mole numbers are treated implicitly:

$$\boldsymbol{n}^{t+1} - \boldsymbol{n}^{t} - \boldsymbol{R}_C^t \boldsymbol{f}_C^{t+1} - \alpha_C \boldsymbol{T}_{Co}^t \boldsymbol{P}_{Co}^{t+1} - \alpha_C \boldsymbol{T}_{Cg}^t \boldsymbol{P}_{Cg}^{t+1} - \boldsymbol{R}_S^t \boldsymbol{f}_S^{t+1} - \boldsymbol{Q}^t = \boldsymbol{0}. \tag{7}$$

In equation (7), $\boldsymbol{n}^t$, $\boldsymbol{f}_C^{t+1}$, $\boldsymbol{f}_S^{t+1}$, $\boldsymbol{P}_{Co}^{t+1}$, and $\boldsymbol{P}_{Cg}^{t+1}$ are the vectors containing the number of moles, central region fugacity, sorbed region fugacity for each component in each grid block, and the vectors of oil pressure in the central region, gas pressure in the central region and the pressure in the sorbed region. $\boldsymbol{R}_C^t$, $\boldsymbol{R}_S^t$, $\boldsymbol{T}_{Co}^t$, and $\boldsymbol{T}_{Cg}^t$ are the transmissibility matrices for the diffusion in the central and sorbed regions, and for the viscous displacement for the oil and gas phases in the central region. The superscript t is the time step index at which the variable is evaluated in the solution of equation (7). The Newton iteration to solve this equation is then

$$\boldsymbol{n}_{k+1}^{t+1} = \boldsymbol{n}_k^{t+1} - \boldsymbol{g}_k \Big/ \left(\frac{\partial \boldsymbol{g}}{\partial \boldsymbol{n}^{t+1}}\right)_k, \tag{8}$$

where the subscript k is the Newton iteration index, $\boldsymbol{g}$ is the vector evaluated using the left-hand-side of equation (7), and $\frac{\partial \boldsymbol{g}}{\partial \boldsymbol{n}^{t+1}}$ is the Jacobian of $\boldsymbol{g}$; that is,

$$\frac{\partial \boldsymbol{g}}{\partial \boldsymbol{n}^{t+1}} = \boldsymbol{I} - \boldsymbol{R}_C^t \frac{\partial \boldsymbol{f}_C^{t+1}}{\partial \boldsymbol{n}^{t+1}} - \alpha_C \boldsymbol{T}_{Co}^t \frac{\partial \boldsymbol{P}_{Co}^{t+1}}{\partial \boldsymbol{n}^{t+1}} - \alpha_C \boldsymbol{T}_{Cg}^t \frac{\partial \boldsymbol{P}_{Cg}^{t+1}}{\partial \boldsymbol{n}^{t+1}} - \boldsymbol{R}_S^t \frac{\partial \boldsymbol{f}_S^{t+1}}{\partial \boldsymbol{n}^{t+1}}. \tag{9}$$

The STONE2 model computes the relative permeability (Ertekin et al., 2001) and the LBC (Lohrenz et al., 1964) model computes phase viscosities. In Equation (8), t is the time step index, $\boldsymbol{n}$ is the vector containing the total number of moles in each grid block for each component, $\boldsymbol{f}$ is the vector containing the fugacities of each component in each grid block, $\boldsymbol{R}$ is the transmissibility matrix containing DGM diffusion coefficients, and $\boldsymbol{Q}$ is the vector containing the boundary condition information as described by Achour and Okuno (2022). The subscripts C and S represent the central and sorbed regions, respectively.

α_C is the central region relative flow coefficient, which accounts for the proximity of each region to the pore wall and the shear stress on the fluid region. α_C is derived by assuming that both regions flow in concentric regions in a tube with the same viscosity. This is a simplifying assumption since the MPTA model predicts that regions have different compositions. The velocity profile as a function of radius $v(r)$ is then (Bird et al., 2001)

$$v(r) = \frac{P_0 - P_L}{4\mu L}\left(R^2 - r^2\right), \tag{10}$$

where P_0, P_L, μ, L, R, and r are the pressure at the upstream and downstream of the tube, viscosity of the fluid, length of the tube, tube radius, and distance from the center of the tube. The flow rate through the central region for the radius extending from 0 to R_C is then the areal integral of the velocity profile

$$Q_C = \pi \frac{P_0 - P_L}{8\mu L} R_C^2 \left(2R^2 - R_C^2\right). \tag{11}$$

The total flow rate of both regions is the areal integral from 0 to R.

$$Q_T = \pi \frac{P_0 - P_L}{8\mu L} R^4. \tag{12}$$

The central region relative flow coefficient is then the ratio of Q_C to Q_T; that is,

$$\alpha_C = 1 - S_S^2, \tag{13}$$

where S_S is the sorbed region volume fraction.

In this paper, the viscous flow in the sorbed region is neglected as a simplifying assumption. In a single-phase flow simulation, it may be simply modeled by adding the term $-(1-\alpha_C)\boldsymbol{T}_S^t \boldsymbol{P}_C^{t+1}$. However, in the presence of multiple phases, it is not clear whether $\boldsymbol{P}_{Cg}^{t+1}$, $\boldsymbol{P}_{Co}^{t+1}$, or a combination of both should be used. Moreover, the relative flow coefficient in the sorbed region $(1-\alpha_C) = S_S^2$ reduces the magnitude of the convection in the sorbed region in favor of that in the central region.

In this paper all flow simulations use a simplified stencil to represent the flow geometry in a hydraulically fractured reservoir (Achour and Okuno, 2022). This stencil represents the volume between a hydraulic fracture (x = 0) and the fracture spacing half-length (x = L). The fracture spacing half-length is modeled using a no-flow boundary condition, and the hydraulic fracture is modeled by a constant pressure and composition boundary condition during injection and constant pressure with upwinded composition during production cycles. During production cycles, upwinding means that the composition in the fracture is set to be equal to that of the central region of the grid block adjacent to it at the previous time-step. Michelsen's (1982 ab) flash calculation at fixed pressure and temperature is carried out without capillary pressure to compute the phase behavior of the oil and gas mixture in the fracture.

It would be interesting to use this model to compare the effectiveness of continuous injection with cyclic injection. The reservoir model described above is designed to model a continuous injection scheme. To model cyclic injection would require a boundary pressure greater than the reservoir pressure during injection cycles and a pressure smaller than the reservoir pressure during production cycles. We found that the resulting pressure gradients caused numerical stability issues, which may require developing a fully implicit version of the simulator.

The models implemented in the flow simulator have been independently validated against experimental data. The capillary pressure is computed using the experimentally measured average pore size and the Parachor correlation extensively studied and validated by Schechter and Guo (1998). The current implementation of the DGM model for diffusion in tight porous media has been validated by Achour and Okuno (2022). The sorption model was validated against experimental measurements for pure CO_2 on a tight reservoir rock by Tovar et al. (2017) and extrapolated to other components using the correlations presented in Appendix A. The model for the impact of capillary pressure on phase behavior is derived from the first and second laws of thermodynamics (Achour and Okuno, 2020, 2021). The PR EOS has been widely used to model mixtures of hydrocarbons and CO_2 (Kumar and Okuno, 2016).

3. Case studies

This section presents case studies of the injection of CO_2 and methane in a Wolfcamp shale. Case 1 focuses on how the injection gas interacts with the in-situ oil and the pore walls without considering transport. This knowledge is the basis for analyzing the flow simulations in Case 2. Case 2 presents the continuous gas injection (CO_2 or methane) into a 1-D reservoir segment representing the volume between a hydraulic fracture and the half distance between two hydraulic fractures in a Wolfcamp shale.

Cases 1 and 2 use the initial reservoir oil represented by a ternary mixture of 30% methane, 30% n-butane, and 40% n-decane. Tables 1 and 2 present the EOS parameters and binary interaction parameters used to compute the phase behavior of mixtures. Table 1 also shows the Parachor coefficients used to compute the interfacial tension with a Parachor exponent of 3.88 (Schechter and Guo, 1998).

3.1. Case 1

This case study presents the simulated sorption for mixtures of the injected gas (CO_2 or methane) with the reservoir oil as calculated by the approximated MPTA method. First, two wall potential models are calibrated to represent the interactions between the fluid and the pore wall. Then, the segregation of the components between the central and sorbed regions is discussed.

Fig. 1 shows the optimal fit of the experimentally measured $\frac{n^{ex}}{m_s}$ for CO_2 sorption for the Wolfcamp shale sample 1 as reported by Tovar et al. (2017). The bold line represents the number of excess moles per mass of rock computed using equation (6) for the entire pore (i.e., $z_1 \leftarrow 0$ and $z_2 \leftarrow z_0$). The density distribution across the pore $\rho(z)$ is calculated using the MPTA method with 100 regions. The DRA parameters are $\varepsilon_0/R = 15$ K and $\beta = 0.35$ for the optimal fit. The measured pore volume per mass of rock is $z_0 = 43.16$ mm^3/g and the pore radius is 7 nm (Tovar et al., 2021).

Appendix A derives the ε_0 correlations for n-alkanes and the ratio of the CO_2 potential parameter ($\varepsilon_{0,CO2}$) to that of methane ($\varepsilon_{0,C1}$) based on experimental data with multiple shale rocks. We estimate the methane wall potential parameter $\varepsilon_{0,C1}$ based on a conservative estimate of 1.4 for the ratio $\varepsilon_{0,CO2}/\varepsilon_{0,C1}$. With this ratio, the wall potential parameter $\varepsilon_{0,CO2}$ is identical to that of ethane $\varepsilon_{0,C2}$ as given by equation (A3) and in the lower quartile of the range of possible values in Table A1. Table 3 shows the values for the DRA parameters calculated for CO_2, methane, n-butane, and n-decane based on the $\varepsilon_{0,CO2}/\varepsilon_{0,C1}$ ratio of 1.4 and equation (A3) in the row labeled as WC1. The bottom row gives another set of parameters labeled as WC2, where the ratio $\varepsilon_{0,CO2}/\varepsilon_{0,C1}$ is set to 2.8 with all other parameters identical to those for WC1. WC2 represents the upper quartile of the range as a higher estimate of the wall potential, where the attractive interactions between CO_2 and the pore walls are stronger.

Fig. 2 shows the composition profile for a Wolfcamp shale containing the initial oil mixture. The compositions of the sorbed and central regions are shown by the straight lines extending from the pore wall ($z/z_0 = 0$) to $z/z_0 = 0.42$ and from $z/z_0 = 0.42$ to the center of the pores ($z/z_0 = 1$). The heaviest component, n-decane, is more attracted to the pore wall and shows a greater concentration in the sorbed region while the lightest component has the weakest attraction to the pore wall and shows a greater concentration in the central region. The intermediate component, n-butane, shows a slight preference for the sorbed region.

To analyze the segregation of components between the two regions, we define a segregation coefficient for each component $\mathscr{S}_i = x_{iC}/x_{iS}$ (i =

Table 1
EOS, interfacial tension, and DRA potential parameters for the components for the case study. ACF stands for acentric factor, V_C for critical volume, and MW for molecular weight.

	z	Pc	Tc	ACF	Parachor	Vc	MW
	mol%	bar	K			cc/mol	g/mol
CO_2	0	73.82	304.21	0.225	82	92.790	44.01
CH_4	30	46.03	190.58	0.0104	74.05	97.959	16.04
C_4H_{10}	30	37.96	425.18	0.201	193.9	251.55	58.12
$C_{10}H_{22}$	40	21.07	617.65	0.49	440.69	595.25	142.29

Table 2
Binary interaction parameters for the components for the case study.

	CO_2	CH_4	C_4H_{10}	$C_{10}H_{22}$
CO_2	0	0.1	0.1257	0.0942
CH_4	0.1	0	0.027	0.042
C_4H_{10}	0.1257	0.027	0	0.008
$C_{10}H_{22}$	0.0942	0.042	0.008	0

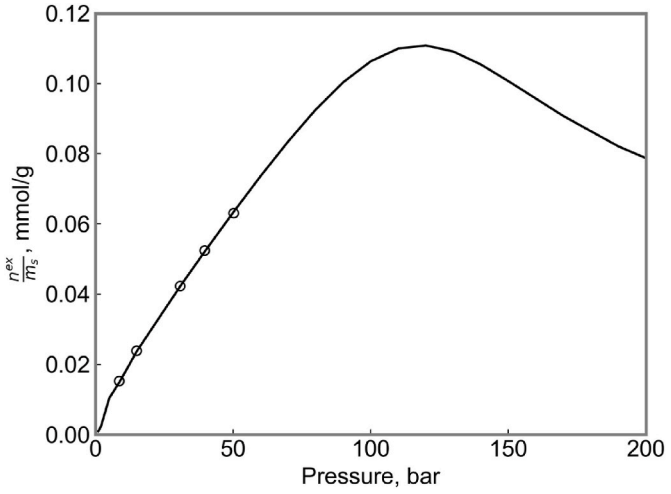

Fig. 1. Calibration of the sorption isotherm for CO_2 for sample 1 Wolfcamp shale using the data of Tovar et al. (2017) at 347 K (365 °F). The experimental data are hollow circles, and the MPTA calculation is the bold line. Copyright 2023, Society of Petroleum Engineers Inc. Reproduced with permission of SPE. Further reproduction prohibited without permission.

Table 3
DRA potential parameters for fluid simulated in case 2.

Variable	Unit	CO_2	CH_4	C_4H_{10}	$C_{10}H_{22}$
ε_{WC1}/R	K	15	10	24	51
ε_{WC2}/R	K	30	10	24	51

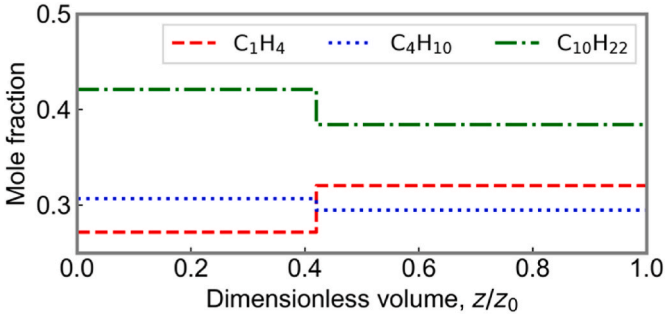

Fig. 2. Oil composition profiles across a Wolfcamp shale pore. The oil contains 30% C_1, 30% nC_4, and 40% nC_{10}. The temperature is 347 K and the pressure is 110 bar. The composition of the sorbed region is shown using straight lines from the pore wall ($z/z_0 = 0$) to $z/z_0 = 0.42$, and the composition of the central region is shown using straight lines from $z/z_0 = 0.42$ to $z/z_0 = 1$. Both regions display a single liquid phase.

$1, \ldots, N_c$), in which x_{iC} and x_{iS} are the overall mole fractions of component i in the central and sorbed regions, respectively. The segregation coefficients based on Fig. 2 are then 1.179 for methane, 0.9603 for n-butane, and 0.9132 for n-decane.

Fig. 3abc show the compositions in the central and sorbed regions for oil/CO_2 mixtures in a quaternary diagram with WC1 and WC2, and oil/methane mixtures in a ternary diagram. The bold line shows the composition in the central region and the dashed line shows the composition in the sorbed region. Thin black dashed lines connect the central- and sorbed-region compositions at 25%, 50%, and 75% injectant (i.e., CO_2 or methane). Those lines connect equilibrium compositions in the two regions and are referred to as "sorption tie-lines" in this analysis. Black lines indicate that the region is in a liquid state, blue lines indicate that the region is in a 2-phase envelope, and a red line indicates

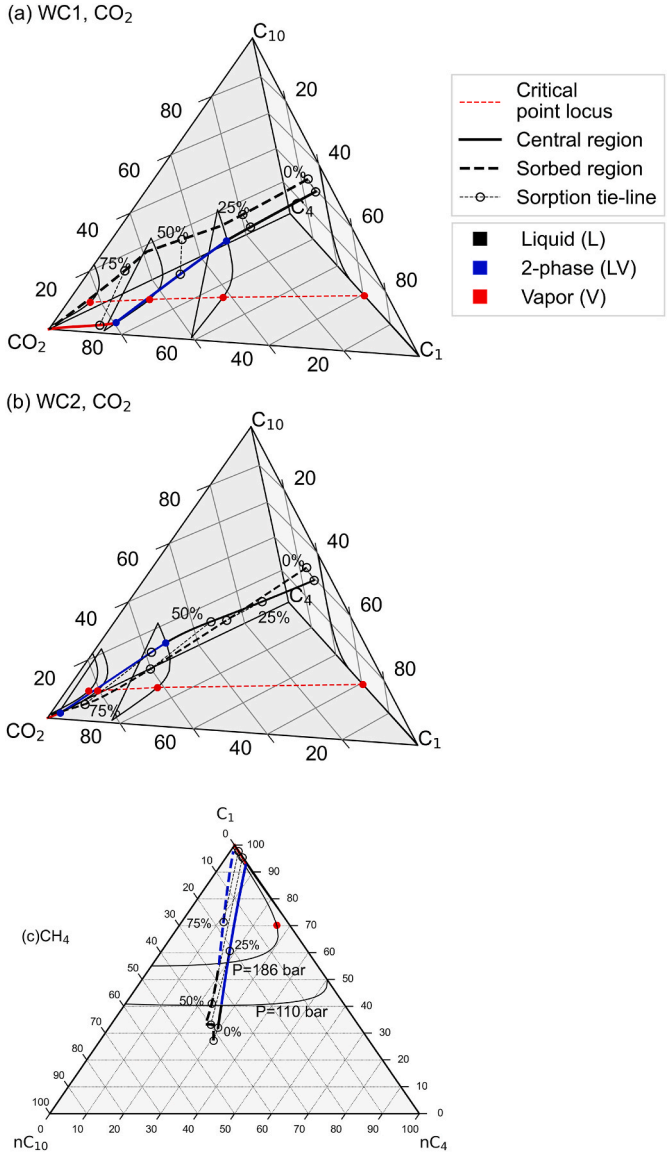

Fig. 3. Compositions in the central and sorbed resions for oil/CO_2 mixtures in a quaternary diagram with (a) WC1 and (b) WC2, and (c) oil/methane mixtures in a ternary diagram. The bold line shows the composition in the central region and the dashed line shows the composition in the sorbed region. Thin black dashed lines connect the central- and sorbed-region compositions at 25%, 50%, and 75% injectant (CO_2 or methane). Black lines indicate a liquid state and blue lines indicate a 2-phase state. Ternary and quaternary diagrams were constructed using the python-ternary (Harper et al., 2019) and python-quaternary (Achour, 2023) libraries, respectively.

that the region forms 100% vapor at equilibrium.

Fig. 3a shows very little segregation of the components between the central and sorbed regions between 0% and 25%. At the 50% CO_2 sorption tie-line, however, the central region is in the two-phase zone and the sorption tie-line appears slightly tilted because the central region contains a greater amount of CO_2 than the sorbed region. This CO_2 segregation occurs because CO_2 tends to be in the vapor phase than in the liquid phase in either region. However, this only occurs with the WC1 model.

Fig. 3b shows that when WC2 is used to model the interaction with the pore walls, the trajectories of the sorbed- and central-region compositions are significantly different from those with WC1 (Fig. 3a). As more CO_2 is added to the mixture, the central- and sorbed-region lines rotate mainly because CO_2 transfers from the central to the sorbed region, and nC_{10} transfers from the sorbed region to the central region. The sorption tie-lines clearly show the increased concentration of CO_2 in the sorbed region. The sorption tie-line does not tilt when the central region crosses the phase envelope as opposed to WC1 in Fig. 3a. Because of the CO_2 segregation into the sorbed region, it takes more CO_2 for the central region to cross the phase envelope. On the 50% CO_2 sorption line, the central region remains liquid with WC2 whereas it is in the two-phase region with WC1.

Fig. 3c shows that when using C_1 as the injectant, both the central and sorbed regions evaporate when enough methane is injected. Also, the sorption tie-lines show that the pore fluid shows strong segregation of methane into the central region and n-butane and n-decane into the sorbed region. This strong segregation is caused by the existence of a vapor phase even with a small amount of methane.

In summary, Fig. 3abc show that three different types of the sorption tie-lines occur for three different levels of affinity of the injectant for the pore wall. CO_2 is neutral with WC1; CO_2 prefers the sorbed region with WC2; and methane prefers the central sorbed region. These three levels of affinity will be shown to yield different results of the transport simulation in case 2.

Fig. 4 shows $\mathscr{S}$ and vapor-phase saturation (S_V) as a function of the mole fraction of CO_2 (Fig. 4ab) or methane (Fig. 4c) at 110 bar and 347 K. The black bold line, red dashed line, blue dotted line, and green dash-dotted line represent the $\mathscr{S}$ values for CO_2, C_1, C_4, and C_{10}, respectively, on the primary y-axis. The thin black dashed and dotted lines represent S_V in the central region (S_{CV}) and in the sorbed region (S_{SV}) on the secondary y-axis. The wall potential model is WC1 for Fig. 3a and WC2 for Fig. 4b. Fig. 4c does not contain CO_2; therefore, there is no difference between using WC1 and WC2. The relationship between $\mathscr{S}$ and the mole fraction of the injection gas is referred to as "Sx diagram."

In each Sx diagram, a thin horizontal black line represents the neutral segregation, where a component exists at equal mole fractions in both regions. Component i preferentially resides in the central region if $\mathscr{S}_i > 1.0$ (e.g., methane in Fig. 2). Otherwise, it preferentially resides in the sorbed region (n-butane and n-decane in Fig. 2).

Fig. 4ab indicate that the wall potential parameter has a strong influence on the segregation of not only CO_2, but also the other species present in the oil mixture. CO_2 shows a strong affinity for the pore wall and displaces n-butane and n-decane from the sorbed region in Fig. 4b. In particular, n-decane is the most strongly affected component because $\mathscr{S}_{C10}$ becomes even greater than those of the other components within a range of CO_2 mole fractions. Fig. 4b shows the appearance of the gas phase when the mixture contains more than 67% CO_2. This is because CO_2 tends to reside in the sorbed region with the WC2 wall potential model. This will be shown to be the mechanism for a significant increase in the n-decane production rate when CO_2 is injected with the WC2 wall potential model.

Fig. 4ac show that methane and CO_2 as the injection component result in qualitatively similar Sx diagrams with the WC1 wall potential model. The injection component shows a preference for the central region at all mole fractions with a maximum at the dew point, while n-butane and n-decane display the opposite trend. A greater level of

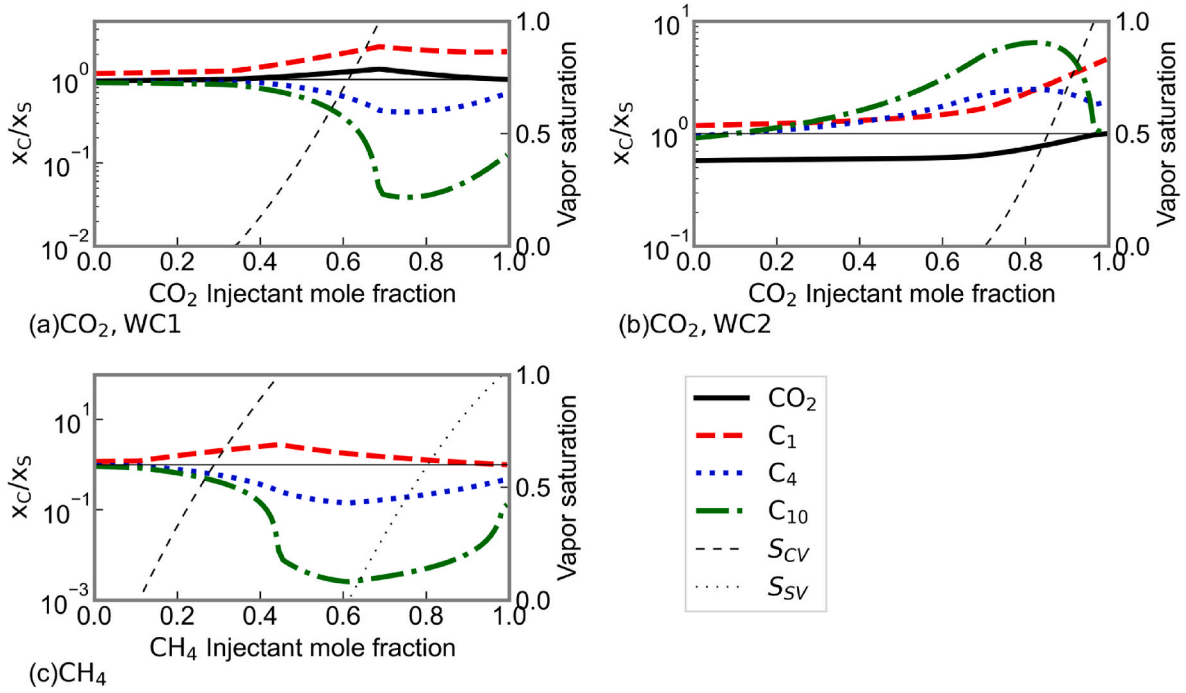

Fig. 4. Segregation coefficient $\mathscr{S} = x_C/x_S$ on the primary y-axis and the vapor phase saturation S_V on the secondary y-axis for oil/solvent mixtures as a function of solvent mole fraction.

compositional segregation is observed with methane (Fig. 4c) than with CO_2 (Fig. 4a) with the WC1 wall potential model. Methane as the injection component causes the vapor phase to appear with a smaller concentration than CO_2 does with the WC2 wall potential model (Fig. 4ab). Fig. 4ac quantitatively show that C_1 displays a stronger preference for the liquid phase in the central region than CO_2 with WC1.

The impact of mixing between the injected component and the reservoir oil is investigated in more detail. We specifically investigate the apparent pressure of the sorbed region, P_S, based on the PR EOS, composition, and density because they fundamentally influence the mass transfer calculated in the simulation. P_S is the apparent pressure that represents the molar density in the sorbed region via the PR EOS and should not be taken as pressure of the fluid near the pore wall.

Fig. 5 presents P_S as a function of the mole fraction of the injection component for CO_2 with WC1 and WC2 and C_1 at 110 bar. With C_1 as the injected component, the sorbed region starts evaporating at 60% C_1. Fig. 5 uses black bold lines and dashed red lines to represent the vapor and liquid phases, respectively. With CO_2 as the injection component,

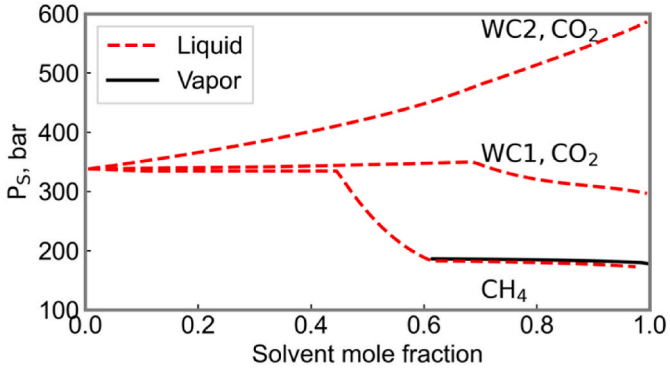

Fig. 5. Apparent sorbed region pressure P_S for oil/solvent mixtures with methane and CO_2 as a solvent. The liquid and vapor pressure are shown with a red dashed line and a dark bold line. In this plot, the liquid pressure of the central region is fixed at 110 bar.

the sorbed region does not display a phase transition, which is why it is shown as a liquid phase with a red dashed line.

With WC2, P_S monotonically increases with CO_2 mole fraction. That is, the stronger interactions between the pore walls and CO_2 cause CO_2 to accumulate in the sorbed region and, therefore, increase in density and P_S.

With WC1, P_S is nearly constant up to the mole fraction of 0.73 for CO_2 and 0.61 for C_1. These concentrations correspond to the dew point in the central region. With the mole fractions above the dew point, the oil/CO_2 mixture displays a single vapor phase with a clear decrease in the apparent sorbed-region pressure P_S with increasing CO_2 mole fraction. That is, the additional moles added to the system display a preference towards the vapor phase rather than the pore wall with the weaker interactions. The main difference between C_1 and CO_2 is that the sorbed region does not evaporate when using CO_2. At 61% added methane, a vapor phase appears in the sorbed region and P_S becomes nearly constant with the addition of C_1.

3.2. Case 2

This case study presents simulation results for continuous CO_2 and methane injection into a tight porous medium. It highlights the importance of properly characterizing interactions of CO_2 with the pore walls relative to n-alkanes. Simulations compute either diffusion/convection or diffusion only for the central region, and only diffusion in the sorbed region. The WC1 model represents the relatively weak interaction of CO_2 with the pore wall, and the WC2 model represents the strong CO_2 interaction with the pore wall. The initial reservoir oil composition, solvent composition, EOS model, and wall potential parameters are the same as those in case 1.

Fig. 6 represents the model used to simulate the CO_2 and methane injection into a hydraulically fractured tight reservoir. The 1-dimensional stencil represents the volume between a hydraulic fracture and the halfway distance between two fractures. The hydraulic fracture is modeled as a constant composition and pressure boundary condition on the left edge of the 1-D stencil. The halfway distance between two fractures is modeled as a no flow/mass transfer boundary on the right

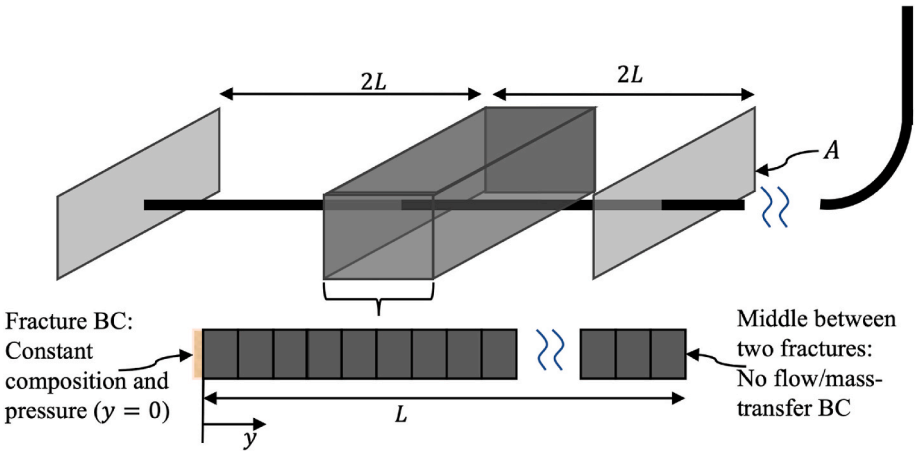

Fig. 6. Schematic for simulation of methane or CO_2 injection into a tight reservoir (Adapted from Achour and Okuno, 2022).

edge.

Table 4 presents the numerical parameters used in this simulation, including petrophysical parameters of the Wolfcamp shale sample 1 as reported by Tovar et al. (2017, 2021). The tortuosity was calculated using the Carman-Kozeny relationship (Peters, 2012a) $\tau = \varphi r_H^2 / 2k$, where φ, k, and r_H are porosity, permeability, and hydraulic radius approximated as the average pore radius r. The simulated 1-D reservoir volume is 9 m^3 and is discretized into 200 grid blocks. Fig. 7 shows the relative permeability curves used to simulate multiphase flow when convection is included for the central region.

Fig. 8 shows the cumulative number of moles of the injected component (CO_2 or C_1) and C_1, C_4, and C_{10} mol produced through counter-current diffusion for four different simulation cases. The black bold lines show the recovered/injected moles when convection is included. The dashed red lines show the recovered/injected moles when only diffusion is included in the simulation. The curves labeled "C_1" show the injected and recovered moles when C_1 is injected. The curves labeled "WC1, CO_2" and "WC2, CO_2" show the injected and recovered moles when CO_2 is injected and the WC1 and WC2 models are used for the wall potential, respectively.

The methane injection and WC1 CO_2 injection cases are diffusion-dominant because the inclusion of convection only slightly increases the injected and produced moles. The observed insensitivity of cumulative injection and production to convection is largely because the boundary and initial conditions have the same pressure. The relative contribution of convection will increase if a large pressure gradient is applied by the boundary condition and if the reservoir is more permeable.

The cumulative amount of injection is significantly smaller when methane is injected as compared with CO_2 with both WC1 and WC2. This is caused by a lower fugacity gradient of methane across the fracture since the initial reservoir oil contains methane, but not CO_2. The cumulative production of n-butane and n-decane is nearly the same for methane and CO_2 with WC1, even though the cumulative amount of methane is substantially smaller than that of CO_2. This indicates that methane is more efficient at extracting moles of hydrocarbons from the reservoir than CO_2 when it has relatively weak interactions with the pore wall. The greater efficiency of C_1 in comparison to CO_2 with WC1 is shown by a greater slope for the C_1 curves than CO_2 curves (Fig. 8e).

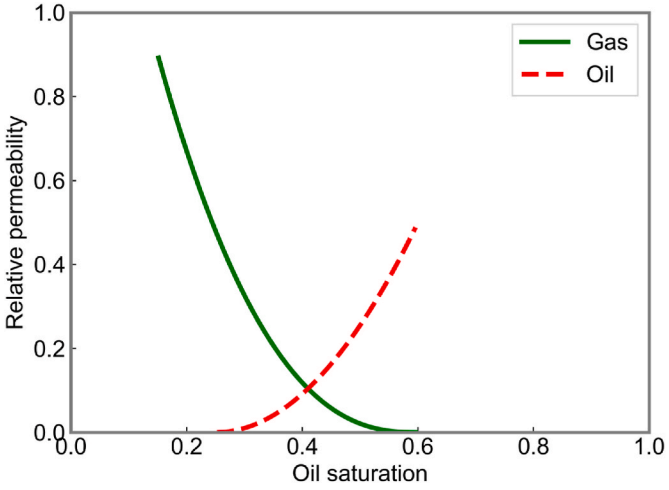

Fig. 7. Oil/gas relative permeability model used in the flow simulation for case 2.

Fig. 8 shows that the most performant injectant was CO_2 with WC2. Fig. 8a shows that CO_2 with WC2 yields the greatest amount of injectant in the reservoir. When convection is included, it also yields the greatest amount of produced C_1, C_4, and C_{10} with the greatest improvement being for heavier alkanes. Moreover, Fig. 8e shows that CO_2 with WC2 yields a greater amount of storage of the injectant for a given amount of production.

The results show that the wall potential substantially affects the simulation results, where WC2 results in a significant increase in cumulative CO_2 injection and recovery of oil components than WC1. As mentioned previously, the main difference between these two wall potential models is that WC2 has a greater wall potential parameter $\varepsilon_{0,CO2}$ than WC1.

Fig. 9 shows the effect of convection on the overall mole fraction profiles after 1500 days of continuous C_1 and CO_2 injection. Fig. 9ab show the overall mole fraction profiles for C_1 injection with and without convection, respectively. Fig. 9cd show the overall mole fraction profiles

Table 4
Petrophysical and numerical parameters for the Wolfcamp shale sample 1 (Tovar et al., 2017, 2021).

φ	k	τ	S_w	γ	r	z_0	A	Δx	N_{GB}	Δt
	μD				nm	mm^3/g	m^2	m		s
10.3%	1.37	1.87	0%	3.88	7	43.16	1	0.045	200	1000

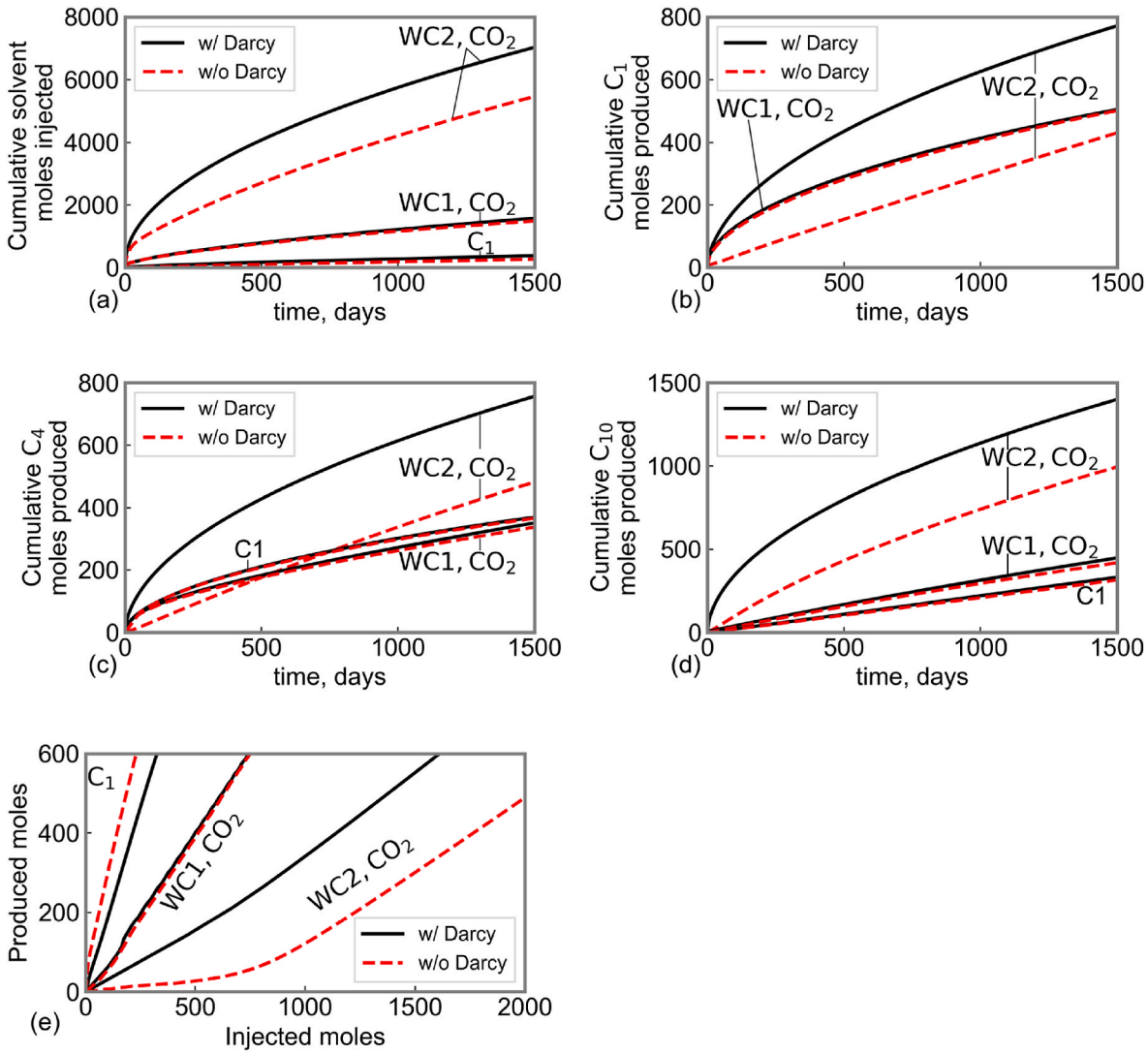

Fig. 8. Simulation results from case 2; (a) cumulative amounts of CO_2/C_1 injected, (b) cumulative amount of C_1 produced produced, (c) cumulative amount of C_4 produced, (d) cumulative amount of C_{10} produced, and (e) the total mole numbers produced with respect to the injected mole numbers in continuous CO_2/C_1 injection for 1500 days for Wolfcamp shales WC1 and WC2. The initial reservoir contains 30% C_1, 30% C_4, and 40% C_{10}. Labels are included in each subplot to describe the solvent injected (i.e., C_1 or CO_2) and the DRA model used for the sorption (i.e., WC1 or WC2). The label does not specify the DRA model used when C_1 is injected because both WC1 and WC2 have the same DRA parameters in the ternary system which does not include CO_2.

for CO_2 injection with WC1 with and without convection, respectively. Fig. 9ef show the overall mole fraction profiles for CO_2 injection with WC2 with and without convection, respectively.

The main difference between Fig. 9e and f is that, when convection is included, the mole fraction of CO_2 increases and the mole fraction of methane, n-butane, and n-decane decrease at the right edge of the 1-D medium. This indicates that the transport is accelerated when convection is included with the stronger interactions of CO_2 with the pore wall (WC2). Fig. 9df show that CO_2 diffuses into the reservoir much faster with WC2 than with WC1.

For C_1 and CO_2 with WC1, plots with and without convection are nearly identical; that is, the contribution of convection to molar flux is negligible in this simulation as indicated in Fig. 8. Fig. 9bd show that the mole fraction of C_1 is relatively flat at 60% near the fracture, whereas the CO_2 mole fraction shows a negative slope. Also, the mole fraction of n-decane is greater near the fracture in Fig. 9b than Fig. 9d.

Fig. 10 shows the pressure profiles for the liquid and vapor phases using a dark bold line and a red dashed line after 1500 days of continuous injection with the WC1 and WC2 models. Fig. 10abc show the pressure profiles for methane and CO_2 injection with WC1 and WC2 with both diffusion and convection. Fig. 10def show the pressure profiles for methane and CO_2 injection with WC1 and WC2 with diffusion only. Fig. 10ghi show the apparent sorbed-region pressure profiles for methane and CO_2 injection with WC1 and WC2 for simulation cases where both diffusion and convection were activated.

Fig. 10abdegh show that the mixing of CO_2 modeled by WC1 or methane with the reservoir oil creates a negligible pressure gradient throughout the reservoir both with and without convection in the central region. The main reason for the small pressure gradient is that, as shown in Fig. 5, mixtures of oil with methane or CO_2 modeled with WC1 do not result in an increase in P_S.

Moreover, Fig. 10abde show a central region fully saturated with a vapor phase within 2.5 m of the fracture and fully saturated with a liquid phase in the rest of the reservoir. The gap between the two curves at 2.5 m represents the capillary pressure and corresponds to a tie-line in composition space (Achour and Okuno, 2023). The transition between the liquid and vapor phases is not an issue when the fugacity is used as the main driving force as in this research because fugacity is continuous at both ends of a tie-line on a phase envelope (Achour, 2023).

Fig. 10bc show that WC2 causes greater pressure gradients than WC1

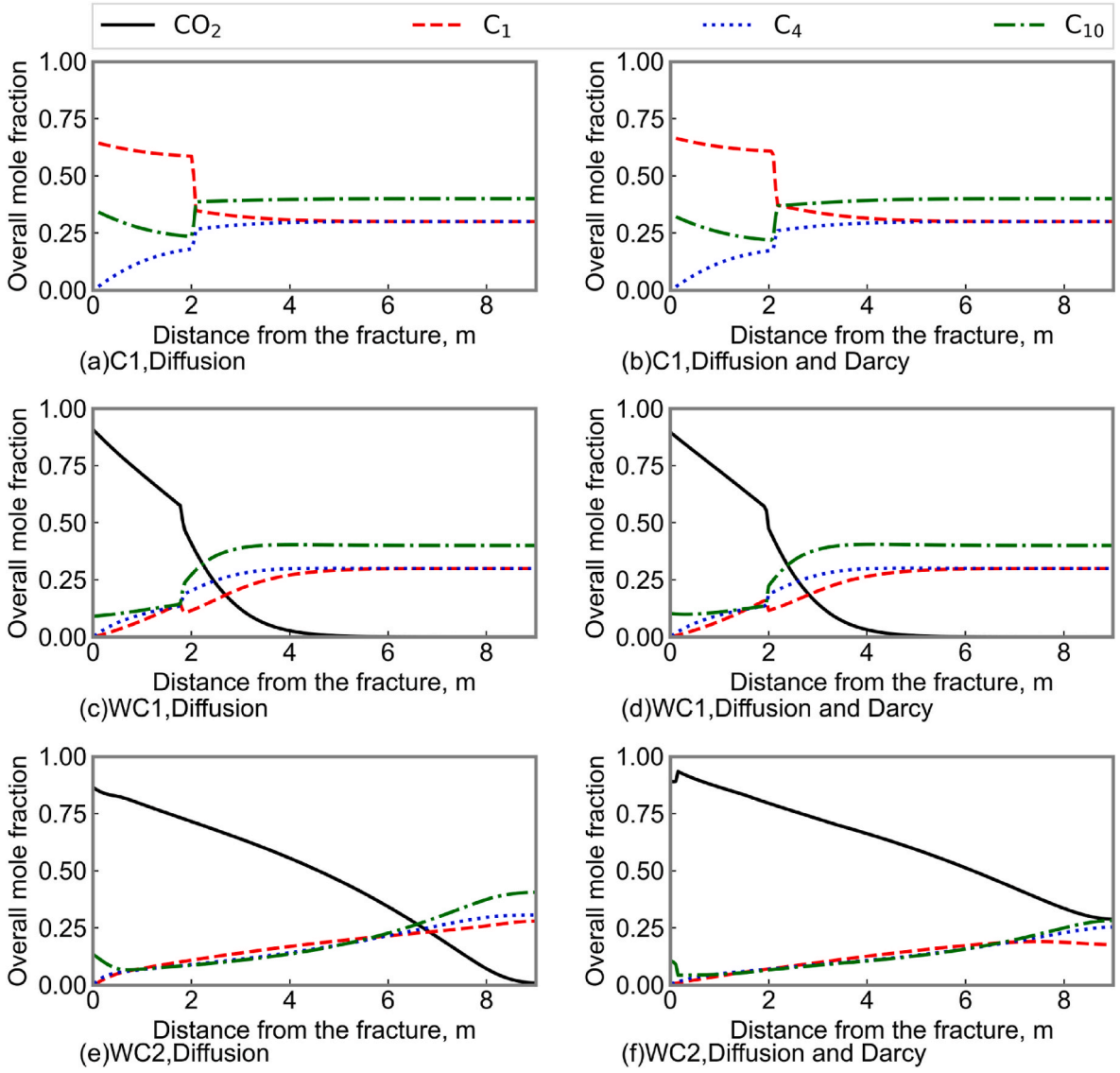

Fig. 9. Composition profiles after 1500 days of continuous injection; (a) the overall mole fraction profiles for methane injected without convection and (b) with convection; (c) the overall mole fraction profiles for CO_2 injection for WC1 without and (d) with convection; and (e) the overall mole fraction profiles for CO_2 injection for WC2 without and (f) with convection.

when CO_2 is injected. The large pressure gradient is caused by the increase in P_S upon mixing between oil and injected CO_2 as shown on Fig. 5. As explained below, this large pressure gradient leads to the effectiveness of CO_2 injection with WC2 in comparison with methane injection or CO_2 injection with WC1.

One important aspect of the DGM diffusion model is that the net flow direction is determined by the pressure gradient (Achour and Okuno, 2022) in both the central and sorbed regions as given by

$$\sum_{i=1}^{N_c} \frac{\dot{n}_i}{Đ^{e}_{iM}} = -\frac{\nabla P}{RT}, \tag{14}$$

where $i = 1,\ldots,N_c$, $\dot{n}_i$ and $Đ^{e}_{iM}$ are the molar flux and effective Knudsen diffusion coefficient for component i, P is the pressure, R is the universal gas constant, and T is the temperature. In the case of CO_2 injection with WC2, the affinity of CO_2 for the pore wall causes it to accumulate in the sorbed region, increasing its density and P_S near the fracture as shown in Fig. 10i. This causes a pressure gradient that further accelerates the diffusion of CO_2 and other oil components through the sorbed region according to equation (14). This accumulation of oil components deep in the reservoir through pressure-driven diffusion in the sorbed region then increases the density of the oil in the central region through the equilibrium as dictated by the MPTA (equation (1)). This causes an increase in the pressure of the central region deep in the reservoir and creates a positive pressure gradient in the central region. This positive pressure gradient enhances the transport through counter-current diffusion and convection. That is why the cumulative recovery of all components for CO_2 injection with WC2 increases significantly when convection is activated. This entire process creates a flux cell between the central and sorbed regions as shown by the schematic in Fig. 11, and enhances the transport of CO_2 solvent into the reservoir and that of the oil components.

Fig. 12 shows the impact of solvent composition and the ratio $\varepsilon_{0,CO2}/\varepsilon_{0,C1}$ on the mole fraction profiles after 1500 days of continuous solvent injection. Fig. 12ab respectively show the central and sorbed regions for the mole fraction profile for the case of continuous methane injection. Fig. 12cd respectively show the central and sorbed regions for the mole fraction profile with WC1. Fig. 12ef respectively show the central and sorbed regions for the mole fraction profile for WC2. Note that Fig. 9bdf show the overall mole fractions corresponding to Fig. 12.

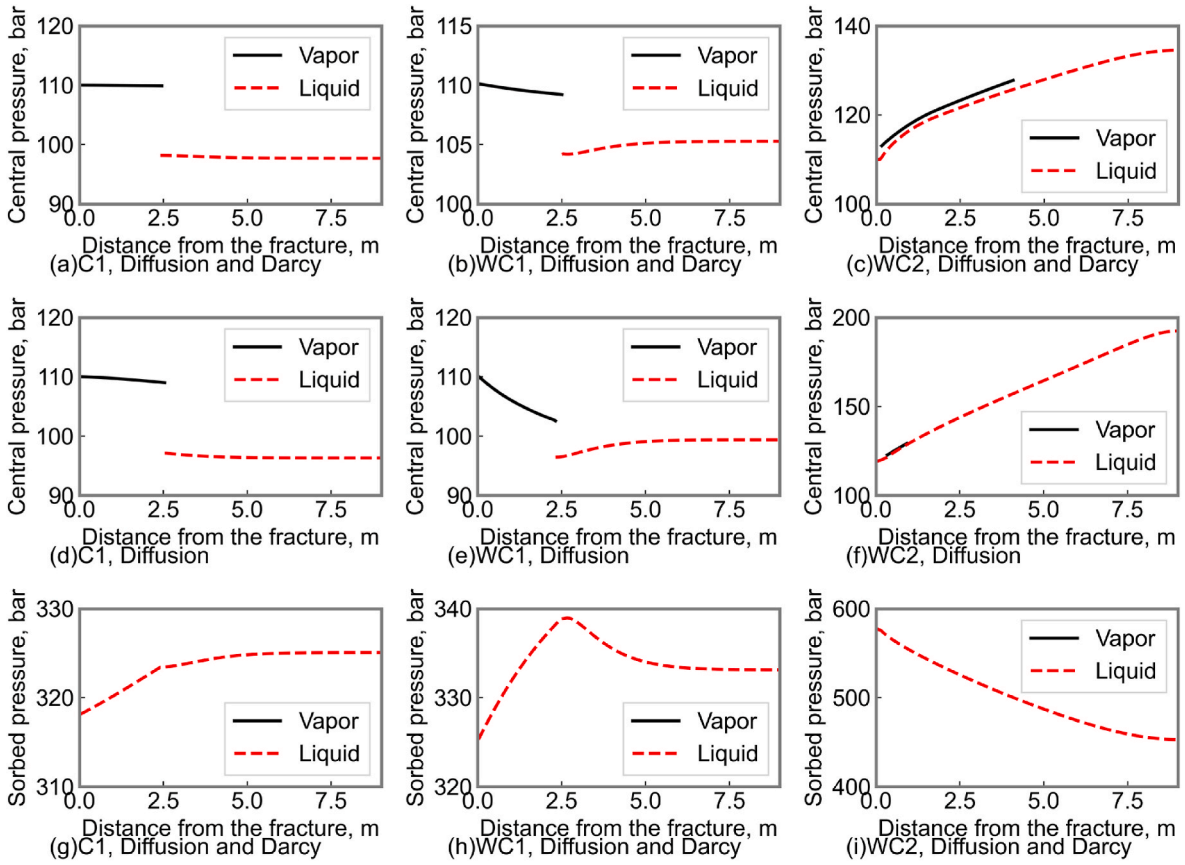

Fig. 10. Pressure profiles for the central and sorbed regions in case 2 at 1500 days. The gas phase is shown with a black bold line and the liquid phase with a red dashed line. Central-region pressures for (a) Methane, (b) CO_2 with WC1, and (b)CO_2 with WC2 with diffusion and convection; central-region pressures for (d) methane, (e) CO_2 with WC1, and (f) CO_2 with WC2 without convection; sorbed-resion pressure for (g) methane, (h) CO_2 with WC1, and (i) CO_2 with WC2.

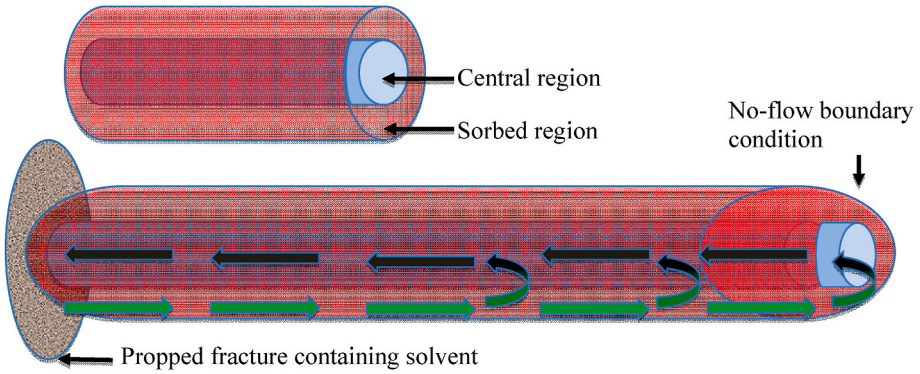

Fig. 11. Schematic showing surface diffusion/convection cell recovery mechanism for CO_2 injection with WC2 model.

After 1500 days of continuous methane and CO_2 injection with WC1, the central region for all grid blocks within the first 2.2 m are saturated with a vapor phase. In the case of methane injection, all components show greater tendencies to segregate between the central and sorbed regions than when CO_2 is injected with WC1. Fig. 12a shows that the central region is almost fully saturated with methane when methane is injected. Fig. 12c shows that when WC1 is used, the high mole fraction of injected CO_2 in the central region near the fracture decreases with distance from the fracture and is only slightly greater than the CO_2 mole fraction in the sorbed region. This is because the CO_2 segregation coefficient is much closer to the neutral line of $\mathscr{S} = 1$ in Fig. 4a. The n-decane mole fraction in the sorbed region is also much greater when injecting methane than CO_2. As was shown by Achour and Okuno (2023), segregation enhances the transport through diffusion. That is why the methane injection results in a similar recovery of n-decane and n-butane to the CO_2 injection, although the methane injection rate is much smaller as shown in Fig. 8.

With both WC1 and WC2, CO_2 exists in both regions, but it concentrates more in the central region for WC1, and in the sorbed region for WC2. Fig. 12d shows that the dominant component of the sorbed region is C_{10} with WC1. However, when the CO_2 wall potential is increased to WC2 (Fig. 12f), the CO_2 mole fraction in the sorbed region increases by displacing C_{10} into the central region causing the counter-current transport of CO_2 and C_{10}. The greater CO_2 wall potential (WC2 in Fig. 12cd) increases the CO_2 mole fraction, density and P_S, all of which enhance transport through the sorbed region. This is further supported

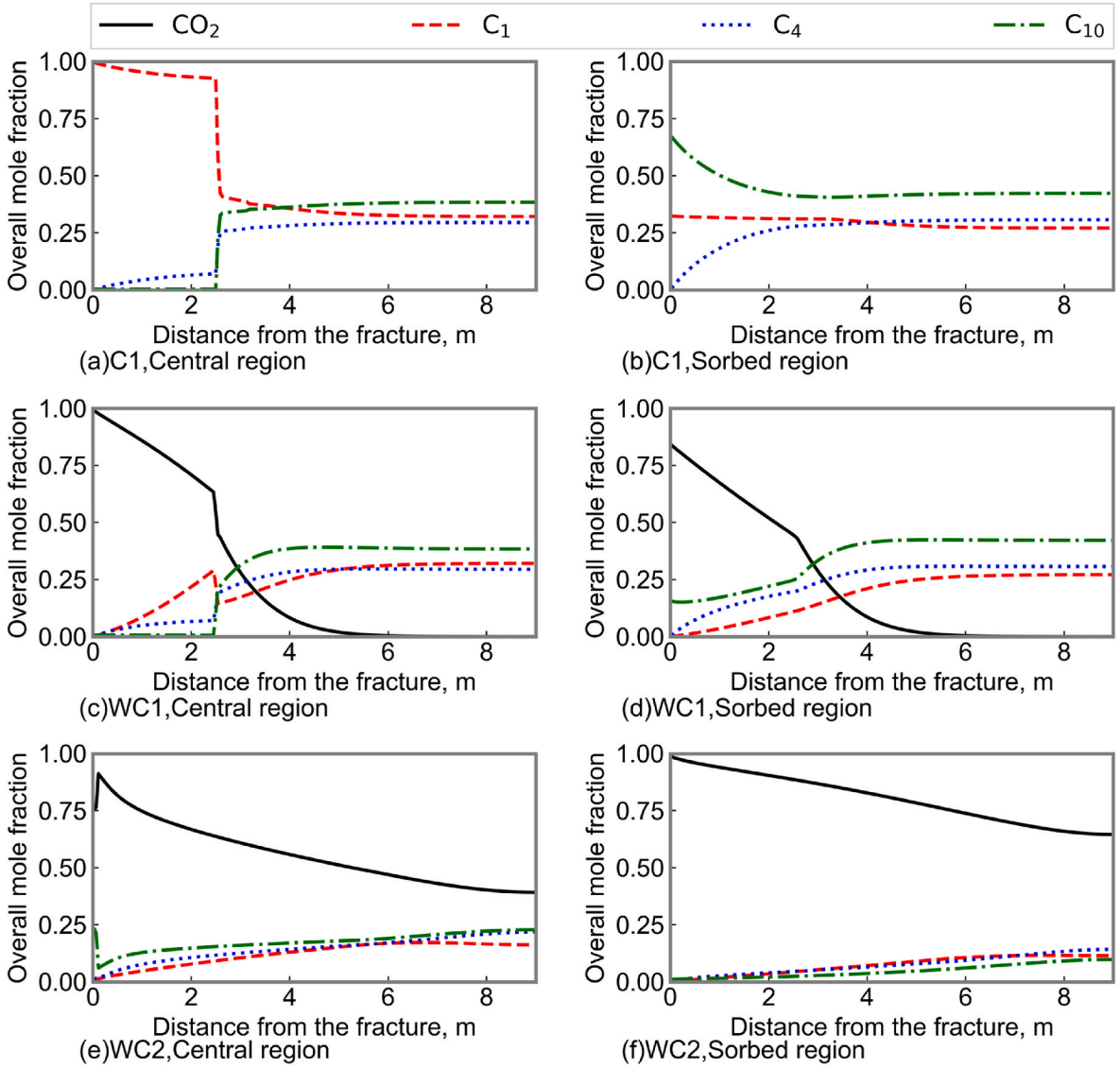

Fig. 12. Composition profiles after 1500 days of continuous CO_2 and methane injection. The (a) central and (b) sorbed region composition profiles are shown for the case of methane injection. The WC1 (c) central and (d) sorbed region mole fraction profiles for CO_2 injection. The WC2 (e) central and (f) sorbed region mole fraction profiles for CO_2 injection.

by the relatively high values of n-decane segregation coefficient on the Sx diagrams in Fig. 4b.

The findings in this research are fundamentally important and novel because they give a detailed analysis of compositional transport and fluid/rock interactions in gas EOR in tight reservoirs. For field applications, sorption measurements of methane and CO_2 with reservoir rocks can be used to obtain the ratio $\varepsilon_{0,CO2}/\varepsilon_{0,C1}$. This ratio is expected to indicate the performance of CO_2 as the injection gas; specifically, a higher value would yield a greater oil recovery. Also, the models can be implemented in a reservoir simulator as was done in this paper, to quantify the recovery factor for a specific reservoir. Results in this research highlight the importance of rock/fluid interactions, in addition to the importance of fluid/fluid interactions.

The impact of phase compositions and sorption on the rock wettability was not explicitly accounted for in this research. Wettability is often quantified by the contact angle θ given by Young-Dupré equation (Peters, 2012b)

$$\cos\theta = \frac{\sigma_{vs} - \sigma_{ls}}{\sigma_{lv}} \tag{15}$$

where σ_{vs}, σ_{ls}, and σ_{lv} are the interfacial tensions between the vapor and solid phases, between the liquid and solid phases, and between the liquid and vapor phases, respectively. In the equation above, the solid-fluid interfacial tensions are thermodynamically linked with the excess moles by the Gibbs adsorption isotherm

$$d\sigma_{js} = -\sum_{i=1}^{N_c} n_{ij}^{ex} d\overline{G}_i \tag{16}$$

where j = L and V, and $\overline{G}_i$ is the partial molar Gibbs free energy of component i ($i = 1, \ldots, N_c$).

Based on Equation (16), the WC2 model makes the rock surface attract CO_2 more than WC1. The flow simulations show a phenomenon akin to capillary imbibition of CO_2 into the reservoir when WC2 is used. However, the Gibbs adsorption isotherm was not used to update the contact angle during the simulation. The rock surfaces were assumed to be strongly liquid-wet in all simulations when calculating the capillary pressure.

Properly accounting for the effect of sorption on the contact angle using the Gibbs adsorption isotherm would require a numerical

integration of equation (16) where each discrete interval would require MPTA flash calculations. A reduced model would be necessary to approximate the Gibbs adsorption isotherm within a reasonable runtime.

4. Conclusions

This paper presented simulation studies of continuous injection of CO_2 and methane into a tight oil reservoir, which involved isothermal multicomponent diffusion-convection including capillary pressure and sorption. The 1-D reservoir model represented Wolfcamp shale with a ternary mixture of methane, n-butane, and n-decane as the initial oil at 347 K and 110 bar. The simulator used the DGM for diffusion and the approximated MPTA method to compute the equilibrium in two concentric regions across each pore in tight porous media. The analysis in this research focused mainly on the impact of pore wall potential on the multicomponent diffusion-dominant transport in gas EOR (CO_2 or methane) in tight formations. The main conclusions are as follows.

- Simulation results highlighted the importance of properly characterizing the reservoir rock through sorption measurements for both CO_2 and n-alkanes. Strong attractive interactions between CO_2 and pore walls nearly doubled the injection rate of CO_2 and the production rate of n-decane (the heaviest component) by displacing it from the pore wall. This strong attraction caused CO_2 to penetrate the tight porous medium deeper and saturate the sorbed region.
- Mixing of injectant with reservoir oil resulted in local changes in molar density and pressure. These pressure gradients were caused by the combined interactions of the injectant with the reservoir oil and with the pore wall. Inclusion of convection tends to dissipate these pressure changes and impact the recovery/injection rates.
- With the relatively weak interaction between the injected gas and the pore wall, the mole fraction of the injected gas and the fluid density in the sorbed region were smaller than those in the central region. This caused small apparent pressure gradients and therefore a small effect on the injection and recovery rates. This was shown for both methane and CO_2 with the wall potential model "WC1."
- Methane was shown to produce more oil per mole of injectant than CO_2 with weak pore wall interactions (WC1).
- With the relatively strong attractive interactions, the CO_2 mole fraction and the fluid density in the sorbed region caused a large apparent pressure in the sorbed region. During flow simulation, this increase in apparent pressure upon mixing enhanced the diffusion of CO_2 into the reservoir through the sorbed region and also the transport of oil components in the opposite direction through the central region (i.e., countercurrent transport of segregated components). These strong gradients in apparent pressure (i.e., molar density) caused a greater impact of convection on the cumulative CO_2 injected and oil moles recovered.
- Equilibrium MPTA calculations showed that in the case of strong interactions between CO_2 and the pore walls, CO_2 displaced heavy components from the pore walls through the liquid phase. However, in the presence of a gaseous phase, CO_2 preferentially segregated into the vapor phase at the center of the pore.

Credit author statement

Sofiane H. Achour: Methodology, Validation, Formal analysis, Investigation, Data curation, Writing – original draft, Visualization. Ryosuke Okuno: Conceptualization, Methodology, Validation, Formal analysis, Resources, Writing – review & editing, Supervision, Project administration, Funding acquisition

Declaration of competing interests

The authors declare that they have no known competing financial interests or personal relationships that could have appeared to influence the work reported in this paper.

Data availability

Data will be made available on request.

Acknowledgements

We acknowledge the support from the members of the Energi Simulation Industrial Affiliate Program on Carbon Utilization and Storage (ES Carbon UT) at the Center for Subsurface Energy and the Environment at the University of Texas at Austin. Ryosuke Okuno holds the Pioneer Corporation Faculty Fellowship in the Hildebrand Department of Petroleum and Geosystems Engineering at The University of Texas at Austin.

Appendices.

Appendix A

The validation of the segregated flow simulation is very challenging because no previous publication contains enough data to properly calibrate all the necessary models. One way to proceed with the current research was to calibrate model parameters based on different experiments with Wolfcamp shale and other rock samples.

Based on Monsalvo and Shapiro (2007), DRA potential ε_0 for activated carbon has a linear function of carbon number *CN*.

$$\varepsilon_0 / R = 0.4300CN + 0.6304\ K. \tag{A1}$$

Based on the literature data gathered by Sandoval et al. (2018), DRA potential ε_0 for Marcellus shale has a linear function of carbon number *CN*.

$$\varepsilon_0 / R = 218.2CN + 288.4\ K. \tag{A2}$$

Based on the proportionality between the slopes and y-intercepts in equations A1 and A2, a general linear equation was created for the wall potential parameter for a rock containing organic pores

$$\varepsilon_0 / R = \alpha(CN + 1.4), \tag{A3}$$

where α is a calibration parameter to match measured sorption for any single n-alkane component.

Figure A1 shows MPTA calculations of the excess sorbed amount defined as

$$n^{ex} = \int_0^{z_0} \rho - \rho_0 dz \tag{A4}$$

calibrated with experimental data for Marcellus, Longmaxi, and Bowland shales by Ansari et al. (2022). Table A1 shows the DRA parameters used to fit experimental data on Figure A1. Based on Monsalvo and Shapiro (2007), the ratio of the methane wall potential to that of CO_2 for activated carbon is about 1.02. This number is consistent with some high-kerogen shale rocks based on calibrated DRA models with the Marcellus and Longmaxi shale. However, both Bowland shale samples show consistently stronger interactions between CO_2 and the pore wall through a greater ratio of $\varepsilon_{0,CO2}/\varepsilon_{0,C1}$.

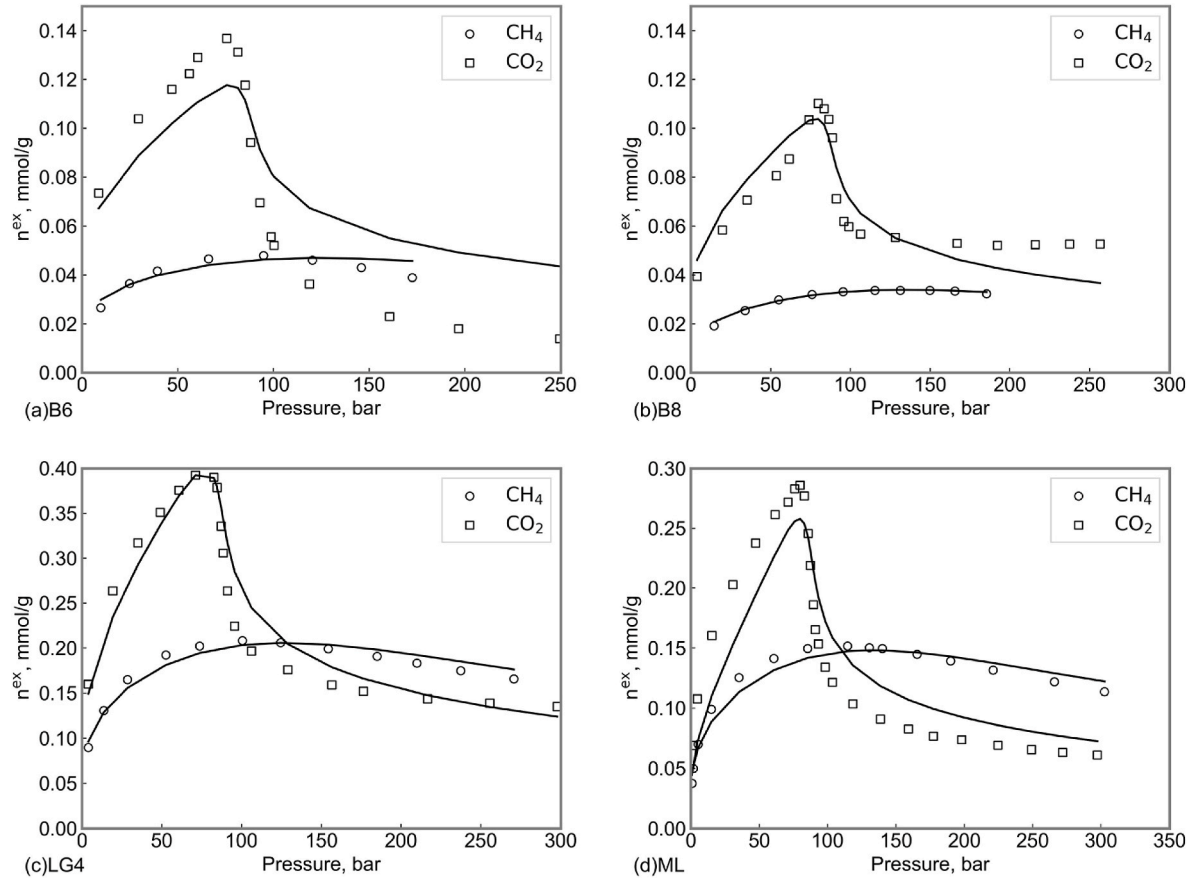

Fig. A1. Calibrated pure CO_2 and CH_4 excess sorbed moles at 40 °C for (a-b) Bowland shale B6 B8, (c) Longmaxi shale LG4, (d) Marcellus shale ML. Hollow circles and squares represent experimental data of sorption by Ansari et al. (2022) for samples (a) B6, (b) B8, (c) LG4, and (d) ML.

Table A1
Summary of calibrated DRA parameters for Longbow, Longmaxi and Marcellus shales.

Shale sample	z_0, mm^3/g	β	$\varepsilon_{0,C1}/R$, K	$\varepsilon_{0,CO2}/R$, K	$\varepsilon_{0,CO2}/\varepsilon_{0,C1}$
B6	20	0.2	4.3	12	2.8
B8	20	0.2	2.3	8	3.5
LG4	50	0.3	45	54	1.2
ML	42	0.3	34	26	0.76

Figure A2 shows the ratio of the DRA potential parameters for n-alkanes and CO_2 to that for methane $\varepsilon_{0,i}/\varepsilon_{0,C1}$ as calculated using the model derived. The ratio was used to compare a normalized value of the DRA wall potential which is independent of the calibration parameter α.

$$\varepsilon_{0,i} \,/\, \varepsilon_{0,C1} = CN/2.4 + 0.583 \tag{A5}$$

where i and CN represent a molecule name and the carbon number. Figure A2 shows that CO_2 interaction with the pore wall can span a wide range of values; it can be weaker than the methane interaction with the pore wall that matches the calibrated values on activated carbon (Monsalvo and Shapiro, 2007), but also can be that of n-heptane.

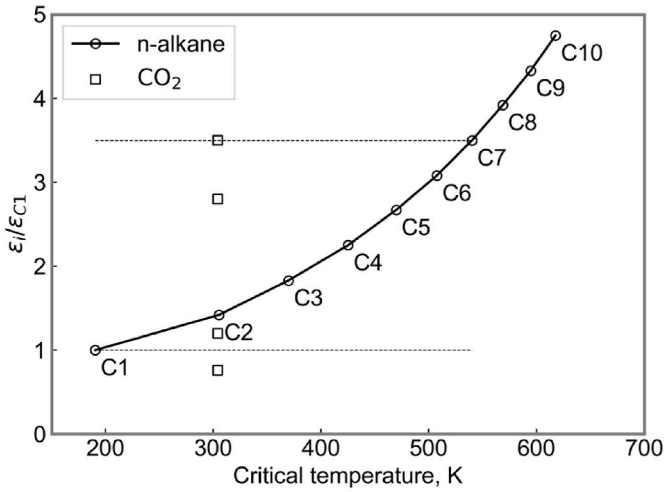

Fig. A2. Plot of calibrated DRA potential for n-alkanes and CO_2.

Appendix B. Comparison between TigReS and a commercial reservoir simulator

This appendix presents a comparison between the models developed in this research and the commercial compositional simulator CMG GEM (Computer Modelling Group, 2020). CO_2 is diffused into a reservoir containing 30% C_1, 30% C_4, and 40% C_{10} through the matrix-fracture interface with WC1 from Case 2. The temperature and initial pressure of both the matrix and the injected CO_2 are set to 347 K and 110 bar.

CMG GEM does not have the option to apply the constant composition and pressure boundary conditions used in Case 2. One approach, which has been used in the literature to emulate this boundary condition, is to place a large grid block with the specified composition and pressure.

In the CMG GEM simulation, therefore, the first grid block from the left is a 100-m-long grid block containing CO_2 at 110 bar. As simulation time progresses, oil diffuses into the boundary grid block. Since the boundary grid block initially contains a large amount of CO_2, the decrease in mole fraction of CO_2 in the boundary grid block is negligible.

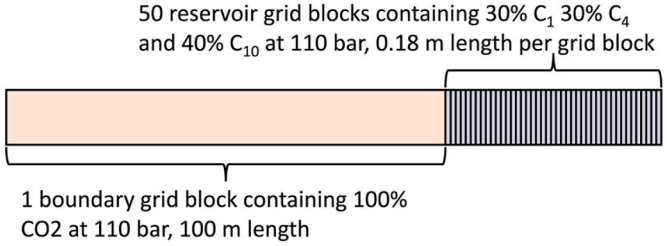

Fig. B1. Schematic for the grids used for CMG GEM to simulate the WC1 CO_2 injection scheme from Case 2. The sizes of grid blocks and number of the reservoir grid blocks are not drawn to scale.

Simulations showed numerical stability and convergence issues when the same time-step and grid block sizes were used as in case 2. Therefore, the CMG GEM simulation was carried out using fifty grid blocks with a length of 0.18 m to represent the 1-D reservoir volume and a maximum time-step size of 0.001 days (86.4 s).

CMG GEM does not have the option to use the dusty gas model for the diffusion of molecules through tight pores, and therefore, we use Fick's law to

model the compositional diffusion in CMG GEM. Equivalent diffusion coefficients based on Fick's law are computed here assuming a diffusion-dominated flow regime. We estimate the Peclet number based on the simulated CO_2 injection with WC1 over 1500 days at the matrix-fracture interface for Case 2 as described below.

According to Perkins and Johnston (1963) for a diffusion-dominant regime, the Peclet number must be less than 0.002. Based on the curves of mole fraction profiles in Fig. 9d, after 1500 days, most of the oil is recovered from the first 4 m. The net cumulative recovery within that time frame is 0.158 mol/day. The cross-sectional area to flow is 1 m^2. The porosity is 0.3%. We estimate the diffusion coefficient based on the definition of the Peclet number (Peters, 2012b):

$$D = \frac{qL}{A\varphi N_{Pe}} = 5.614 \times 10^{-2} \left[cm^2 \Big/ s \right] \tag{B1}$$

We set the diffusion coefficient of methane to the above value in CMG GEM and estimate the diffusion coefficient of CO_2, C_4, and C_{10}. According to the Stokes-Einstein relation, the diffusion coefficient scales with the inverse of viscosity and particle radius $D_i \propto \frac{1}{\mu_i r_i}$ (Reichl, 2016) where μ_i and r_i are the pure substance viscosity and molecular radius for component i ($i = 1, \ldots, N_c$).

First, we estimate the molecular radii based on the EOS. Let us assume that the co-volume defines the smallest molar volume achievable for a substance made of hard spheres. The arrangement of hard spheres that would minimize the volume is the rhombohedral packing (Peters, 2012a) with a porosity of 26%. The molar density for a pure substance at its co-volume would then become

$$\underline{V_i} = \frac{4}{3} \frac{\pi r_i}{1 - 0.26} \left(\frac{10^{-9} m}{nm} \right) \mathcal{N}_A = b_i,$$

where i = 1,..., N_C and $\mathcal{N}_A$ is the Avogadro constant. The radius of molecules can then be estimated as

$$r_i = \left(\frac{b_i \frac{m^3}{mol}}{0.00340885} \right)^{\frac{1}{3}} nm \tag{B2}$$

where i = 1,...,N_C. The estimated molecular radii are presented in Table B1 along with the viscosities of pure substances at the simulation temperature and pressure retrieved from the online NIST database (Lemmon et al., 2018). Table B1 also presents estimated diffusion coefficients based on the Stokes-Einstein scaling.

Table B1
Covolume, molecular radius, viscosity and diffusion coefficients for each component in the CO_2 injection simulation.

	b	r	μ	D
	m^3/mol	Å	cp	cm^2/s
CO_2	2.6655×10^{-5}	1.985	0.023723	3.512×10^{-2}
CH_4	2.6781×10^{-5}	1.988	0.014834	5.614×10^{-2}
C_4H_{10}	7.2450×10^{-5}	2.770	0.12220	4.890×10^{-3}
$C_{10}H_{22}$	1.8961×10^{-4}	3.817	0.53178	8.156×10^{-4}

Sorption is modeled with CMG GEM using the multicomponent Langmuir (ML) model (Computer Modelling Group, 2020)

$$n_i^{ex} = n_{imax}^{ex} \frac{b_i x_i P}{1 + \sum_{j=1}^{N_c} b_j x_j P}, \text{where } i = 1, \ldots, N_c \tag{B3}$$

In Equation B3, n_i^{ex}, n_{imax}^{ex}, and b_i are the number of excess moles per mass of solid rock, the maximum number of excess moles per mass of solid rock, and the sorption equilibrium coefficient component i ($i = 1, \ldots, N_c$). Figure B2 shows the best match of the ML model to excess sorbed moles of CO_2, C_1, C_4, and C_{10} calculated with the WC1 DRA model (Table 3) using a 100-region MPTA equilibrium calculation. Calibrated ML parameters are presented in Table B2. The match appears to be reasonably accurate for CO_2 and C_1. The ML model is unable to properly match the C_4 and C_{10} excess calculated by the MPTA method (Figures B2cd). The main reason for this observation is that C_4 and C_{10} form dense liquids at these conditions and the ML model is unable to model dense fluids with molar volumes close to the covolume parameter of the Peng-Robinson EOS (Achour and Okuno, 2023). The excess is a monotonically decreasing function of pressure in Figure B2cd, but the ML model can only predict increasing functions pressure. To match the MPTA data as closely as possible, the parameters b_{C_4} and $b_{C_{10}}$ from equation (B3) had to be very large values such that the predicted sorption appears to be a straight line when plotted against pressure.

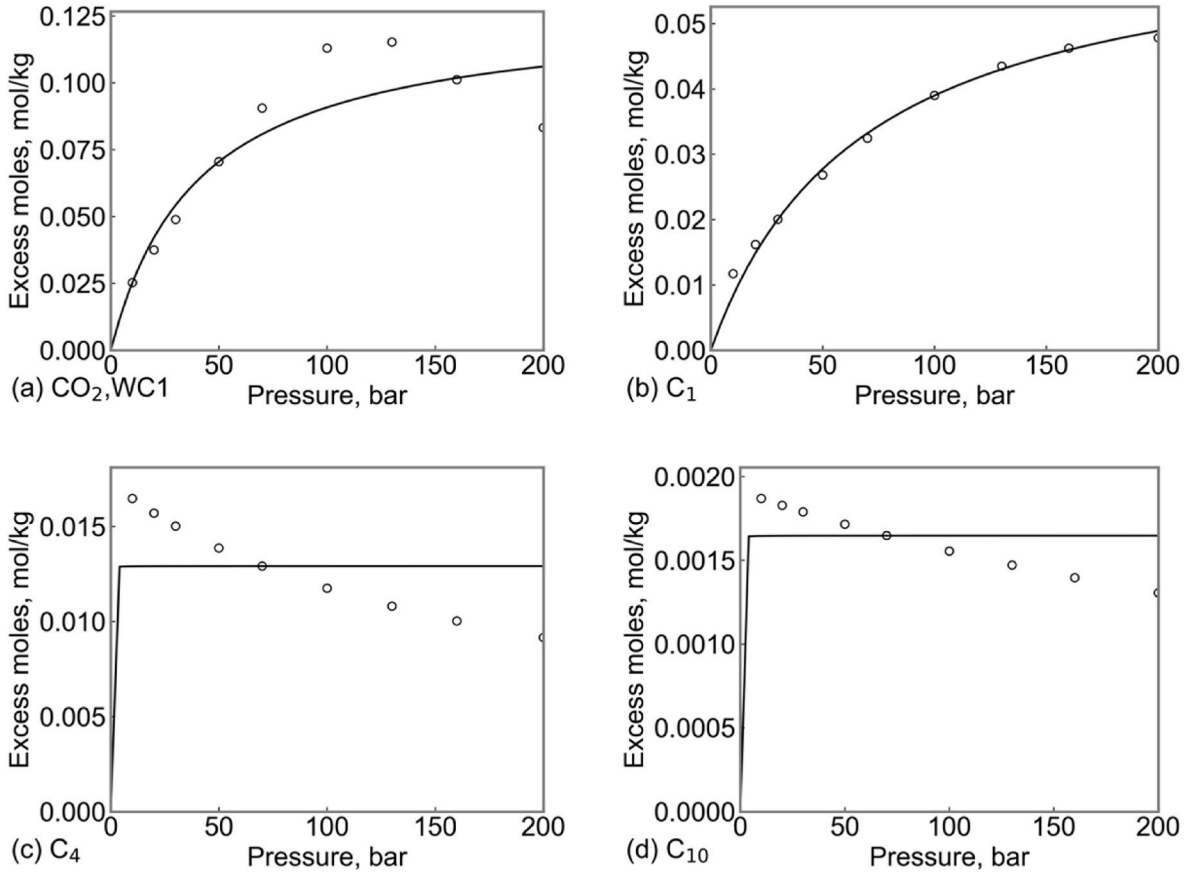

Fig. B2. Match of ML model (bold line) to Wolfcamp shale MPTA equilibrium calculations (hollow circles) for CO_2, C_1, C_4, and C_{10} at 347 K. The MPTA model is the same as that used in case 2 (WC1).

Table B2
ML parameters and their keywords used to approximate the MPTA model for CO_2 diffusion into a Wolfcamp shale containing a ternary mixture of C_1, C_4, and C_{10} at 347 K. ADGSTC and ADGMAXC correspond to b_i and n_{imax}^{ex}, respectively.

		CO_2	CH_4	C_4H_{10}	$C_{10}H_{22}$
ADGCSTC	1/kPa	2.472×10^{-4}	1.471×10^{-4}	1.0	1.0
ADGMAXC	mmol/g	0.1276	0.06551	0.01291	0.001647

Table B3 shows the initial compositional excess moles of the reservoir containing 30% C_1, 30% C_4, and 40% C_{10} as calculated by CMG GEM based on the ML model in Table B2 and the MPTA model. The excess moles are also given as a ratio of excess moles to the total number of moles not adsorbed.

$$\omega_i = \frac{n_i^{ex}}{\sum_{j=1}^{N_c} n_j - n_j^{ex}}, \text{ where } i = 1, \ldots, N_c. \tag{B4}$$

Table B3
Initial compositional excess moles per mass of rock in CMG GEM based on the ML model in Table B2.

		CO_2	CH_4	C_4H_{10}	$C_{10}H_{22}$
ML total excess moles	mmol/grid block	0.0	4.350×10^{-5}	5.508×10^{-2}	7.381×10^{-3}
ML excess moles per total moles	mol/mol	0.0	3.199×10^{-7}	4.051×10^{-4}	5.428×10^{-5}
2-region MPTA excess moles per total moles	mol/mol	0.0	-2.048×10^{-2}	5.124×10^{-3}	5.136×10^{-2}

Table B3 shows that the ML model used in CMG is unable to account for multicomponent segregation where the light components represented by C_1 have negative excess because they segregate at the center of the pore. Instead, the ML model predicts a very small value of excess for C_1. Moreover, because negative excess cannot be modeled by ML, there is less sorption capacity available for C_4 and C_{10} to adsorb. This yields a smaller amount of sorption for C_4 and C_{10}.

The very small value of methane excess is caused by the unusually great values of the ML parameters b_{C_4} and $b_{C_{10}}$, which yield the best match for the negative slope of the liquid hydrocarbons. This causes the denominator in equation (B3) to be significantly greater than the numerator for C_1 and CO_2. This significantly reduces the number of excess moles for light components. The ML is not able to properly model compositional segregation in tight pores.

Figure B3 shows the cumulative compositional recovery for C_1, C_4, and C_{10} from counter-current diffusion and the injected moles of CO_2 by diffusion. The simulated recovery with TigReS was shown in Fig. 8. As opposed to TigReS, CMG GEM predicts that light components represented by methane would be recovered much more than C_4 and C_{10}. The results from TigRes showed that the C_1 C_4 and C_{10} recoveries were very close to each other after 1500 days and C_{10} recovery was greater than that of C_4. This difference occurs because the ML model within CMG GEM does not properly model component segregation across pores and does not account for the composition and density of the fluid near the pore wall on the transport coefficients. The recovered fluid is simulated to be leaner with CMG GEM.

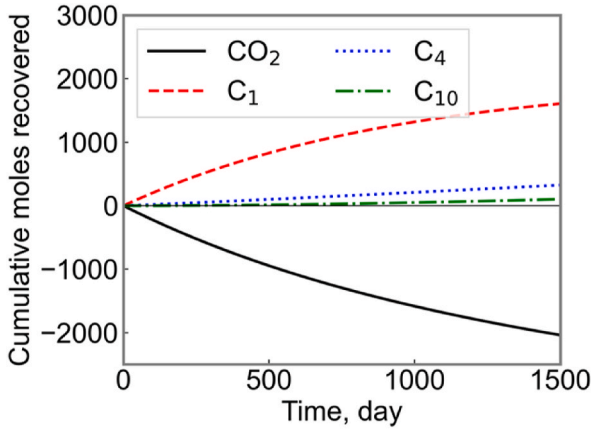

Fig. B3. Cumulative moles recovered during the simulated CO_2 diffusion into a 1-D reservoir containing 30% C_1, 30% C_4, and 40% C_{10} at 347 K with an initial pressure of 110 bar.

References

Achour, S.H., Okuno, R., 2020. Phase stability analysis for tight porous media by minimization of the Helmholtz free energy. Fluid Phase Equil. 520, 112648. https://doi.org/10.1016/j.fluid.2020.112648.

Achour, S.H., Okuno, R., 2021. Two-phase flash for tight porous media by minimization of the Helmholtz free energy. Fluid Phase Equil. 534, 112960. https://doi.org/10.1016/j.fluid.2021.112960.

Achour, S.H., Okuno, R., 2022. Application of multicomponent sorption for diffusive transport in numerical simulation of tight reservoirs. J. Petrol. Sci. Eng. 111262 https://doi.org/10.1016/j.petrol.2022.111262.

Achour, S.H., Okuno, R., 2023. Application of multicomponent sorption for diffusive transport in numerical simulation of tight reservoirs. Geoenergy Sci. Eng. 221, 111262. https://doi.org/10.1016/j.petrol.2022.111262.

Achour, S.H., 2023. Python-quaternary: quaternary plots in Python. Zenodo. https://doi.org/10.5281/ZENODO.7761303.

Akkutlu, I.Y., Fathi, E., 2012. Multiscale gas transport in shales with local kerogen heterogeneities. SPE J. 17 (4), 1002–1011. https://doi.org/10.2118/146422-PA.

Ansari, H., Gong, S., Trusler, J.M., Maitland, G., Pini, R., 2022. Hybrid pore-scale adsorption model for CO2 and CH4 storage in shale. Energy Fuels 36 (7), 3443–3456. https://doi.org/10.1021/acs.energyfuels.1c03723.

Baek, S., Akkutlu, I.Y., 2019. CO_2 stripping of kerogen condensates in source rocks. SPE J. 24 (3), 1415–1434. https://doi.org/10.2118/190821-PA.

Bird, R.B., Stewart, W.E., Lightfoot, E.N., 2001. Transport Phenomena, revised second ed. John Wiley & Sons.

Butt, H.J., Graf, K., Kappl, M., 2003. Physics and Chemistry of Interfaces. John Wiley & Sons.

Clark, A.J., 2009. October. Determination of recovery factor in the bakken formation, mountrail county, ND. In: Presented at the SPE Annual Technical Conference and Exhibition. New Orleans, LA. https://doi.org/10.2118/133719-STU.

Computer Modelling Group (CMG), 2020. GEM Compositional & Unconventional Reservoir Simulator. USER GUIDE C.M.G. Ltd, Calgary, AB, Canada.

Cronin, M., Emami-Meybodi, H., Johns, R.T., 2019. Diffusion-dominated proxy model for solvent injection in ultratight oil reservoirs. SPE J. 24 (2), 660–680. https://doi.org/10.2118/190305-PA.

Cronin, M., Emami-Meybodi, H., Johns, R.T., 2021. Multicomponent diffusion modeling of cyclic solvent injection in ultratight reservoirs. SPE J. 26 (3), 1213–1232. https://doi.org/10.2118/196008-PA.

Dubinin, M.M., 1985. Generalization of the theory of volume filling of micropores to nonhomogeneous microporous structures. Carbon 23 (4), 373–380. https://doi.org/10.1016/0008-6223(85)90029-6.

Energy Information Administration (EIA), 2022. Annual Energy Outlook 2022 with Projections to 2050. Retrieved from. https://www.eia.gov/outlooks/aeo/pdf/AEO2022_Narrative.pdf.

Ertekin, T., Abou-Kassem, J.H., King, G.R., 2001. Basic Applied Reservoir Simulation, vol. 7. Society of Petroleum Engineers, Richardson.

Harper, M., Weinstein, B., Tgwoodcock, S.C., Chebee7i, Morgan, W., Knight, V., Swanson-Hysell, N., Evans, M., Jl-Bernal, ZGainsforth, Badger, T.G., SaxonAnglo, Greco, M., Zuidhof, G., 2019. Marcharper/Python-Ternary: Version 1.0.6. Zenodo. https://doi.org/10.5281/ZENODO.594435.

Hoteit, H., 2013. Modeling diffusion and gas–oil mass transfer in fractured reservoirs. J. Petrol. Sci. Eng. 105, 1–17. https://doi.org/10.1016/j.petrol.2013.03.007.

Kumar, A., Okuno, R., 2016. A new algorithm for multiphase fluid characterization for solvent injection. SPE J. 21 (5), 1688–1704. https://doi.org/10.2118/175123-PA.

Lemmon, E., Bell, I., Huber, M., Harvey, A., McLinden, M., 2018. *NIST Reference Fluid Thermodynamic And Transport Properties Database (REFPROP)* Version 10 - SRD 23. https://doi.org/10.18434/T4/1502528.

Lohrenz, J., Bray, B.G., Clark, C.R., 1964. Calculating viscosities of reservoir fluids from their compositions. J. Petrol. Technol. 16 (10), 1–171. https://doi.org/10.2118/915-PA.

Lund, L., 2014. Decline Curve Analysis of Shale Oil Production: the Case of Eagle Ford. Masters' thesis. Uppsala University.

Ma, M., Emami-Meybodi, H., 2022. September. Diffusion-based multiphase multicomponent modeling of cyclic solvent injection in ultratight reservoirs. In: Presented at the SPE Annual Technical Conference and Exhibition, Houston, TX. https://doi.org/10.2118/210480-MS.

Michelsen, M.L., 1982a. The isothermal flash problem. Part I. Stability. Fluid Phase Equil. 9 (1), 1–19. https://doi.org/10.1016/0378-3812(82)85001-2.

Michelsen, M.L., 1982b. The isothermal flash problem. Part II. Phase-Split calculation. Fluid Phase Equil. 9 (1), 21–40. https://doi.org/10.1016/0378-3812(82)85002-4.

Mohebbinia, S., Wong, T., 2017. Molecular diffusion calculations in simulation of gasfloods in fractured reservoirs. In: Presented at the SPE Reservoir Simulation Conference, Montgomery, Texas, 20-22 February. https://doi.org/10.2118/182594-MS.

Monsalvo, M.A., Shapiro, A.A., 2007. Modeling adsorption of binary and ternary mixtures on microporous media. Fluid Phase Equil. 254 (1–2), 91–100. https://doi.org/10.1016/j.fluid.2007.02.006.

Olorode, O., Amer, H., Rashid, H., 2021. The role of diffusion in primary and enhanced oil recovery from fractured unconventional reservoirs. In: Presented at the Asia Pacific Unconventional Resources Technology Conference, Virtual. https://doi.org/10.15530/AP-URTEC-2021-208387.

Perkins, T.K., Johnston, O.C., 1963. A review of diffusion and dispersion in porous media. SPE J 3 (1), 70–84. https://doi.org/10.2118/480-PA.

Peters, E.J., 2012a. Advanced Petrophysics: Volume 1: Geology, Porosity, Absolute Permeability, Heterogeneity and Geostatistics. Live Oak Book Co, Austin, Texas.

Peters, E.J., 2012b. Advanced Petrophysics: Volume 2: Dispersion, Interfacial Phenomena/Wettability, Capillarity/Capillary Pressure, Relative Permeability. Live Oak Book Co, Austin, Texas.

Reichl, L.E., 2016. A Modern Course in Statistical Physics. Wiley-VCH Verlag GmbH & Co. KGaA, Weinheim, Germany.

Robinson, D.B., Peng, D.Y., 1978. The Characterization of the Heptane and Heavier Fractions for GPA Peng-Robinson Programs. Gas Processors Association Research Report, Tulsa, Oklahoma.

Sandoval, D.R., Yan, W., Michelsen, M.L., Stenby, E.H., 2018. Influence of adsorption and capillary pressure on phase equilibria inside shale reservoirs. Energy Fuels 32 (3), 2819–2833. https://doi.org/10.1021/acs.energyfuels.7b03274.

Shapiro, A.A., Stenby, E.H., 1998. Potential theory of multicomponent adsorption. J. Colloid Interface Sci. 201 (2), 146–157. https://doi.org/10.1006/jcis.1998.5424.

Schechter, D.S., Guo, B., 1998. Parachors based on modern physics and their uses in IFT prediction of reservoir fluids. SPE Reservoir Eval. Eng. 1 (3), 207–217. https://doi.org/10.2118/30785-PA.

Shojaei, H., Jessen, K., 2014. Diffusion and matrix-fracture interactions during gas injection in fractured reservoirs. In: Presented at the SPE Annual Technical Conference and Exhibition, Tulsa, Oklahoma, 12–16 April. https://doi.org/10.2118/169152-MS.

Tovar, F.D., Barrufet, M.A., Schechter, D.S., 2021. Enhanced oil recovery in the Wolfcamp shale by carbon dioxide or nitrogen injection: an experimental investigation. SPE J. 26 (1), 515–537. https://doi.org/10.2118/204230-PA.

Tovar, F.D., Barrufet, M.A., Schechter, D.S., 2017. Non-destructive measurement of porosity, compressibility and gas sorption in core plugs from the Wolfcamp shale. In: Presented at the SPE Latin America and Caribbean Petroleum Engineering Conference, Buenos Aires, Argentina. https://doi.org/10.2118/185604-MS.

Yanze, Y., Clemens, T., 2012. The role of diffusion for nonequilibrium gas injection into a fractured reservoir. SPE Reservoir Eval. Eng. 15 (1), 60–71. https://doi.org/10.2118/142724-PA.